BCS-BEC crossover and superconductor-insulator transition in Hopf-linked Graphene layers: Hopfene

Shinichi Saito[1] **& Isao Tomita**[1,2]

[1]Sustainable Electronic Technologies Research Group, Electronics and Computer Science, Faculty of Engineering and Physical Sciences, University of Southampton, SO17 1BJ, UK.

[2]Department of Electrical and Computer Engineering, National Institute of Technology, Gifu College, 2236-2 Kamimakuwa, Motosu, Gifu 501-0495, Japan.

E-mail: S.Saito@soton.ac.uk

June 2019

Abstract. We have proposed a topological carbon allotrope, named Hopfene, which has three-dimensional ($3D$) arrays of Hopf-links to bind $2D$ Graphene layers both horizontally and vertically without forming strong σ bonds between layers. Tight-binding calculations show unique band structures of this crystal, which predicts semi-metal characteristics with the existence of both Weyl and Dirac Fermions depending on the Fermi energy. Here, we have theoretically examined superconductivity of Hopfene based on the attractive Hubbard model. Regardless of its simplicity of the model, we found non-trivial competitions between Hartree-Fock mean-field contributions and Cooper-paring interactions to open semiconductor and superconducting energy gaps, respectively. Consequently, the superconducting order parameters are significantly reduced at every quarterly doping concentration, where the system is in the close vicinity of the quantum critical point, and we found superconductor-insulator transition in the strong coupling limit. Upon doping, we confirmed a classical scenario of a smooth crossover from weak coupling Bardeen-Cooper-Schrieffer (BCS) superconductivity to strong coupling Bose-Einstein Condensation (BEC) of preformed pairs by increasing the interaction strength. We think the proposed Hopfene is a useful platform to investigate the impacts of the topological nature of the Fermi surfaces on the superconductivity and other orders, including charge-density-waves and magnetic orders, and possible quantum phase transitions among them.

Submitted to: *2D Mater.*

1. Introduction

The discovery of superconductivity by Onnes [1, 2] was a mystery for a long time and it was finally solved by Bardeen, Cooper, and Schrieffer (BCS) after a half century from the discovery based on quantum-mechanical many-body field theory[3–6]. Besides its technological significance of superconductivity, the mechanism was astonishing: the

broken $U(1)$ gauge symmetry led to the formation of the energy gap, Δ, leading to the macroscopic coherent state, which allows the persistent currents and Meissner effect[3–7]. Nambu was inspired by the BCS theory and generalised the concept of broken symmetry[8] to explain the emergence of mass in elementary particles. He compared the quasi-particle dispersion, $E^2 = \epsilon^2 + |\Delta|^2$, after the onset of the superconductivity with the energy spectrum obtained by Einstein's special theory of relativity, $E^2 = (cp)^2 + (mc^2)^2$, where c is the speed of light and m is the mass of the particle. He suggested that the original massless particle with the energy, $\epsilon = cp$, and the momentum of p would acquire the mass by the formation of the energy gap $|\Delta| = mc^2$. He also established the generation of new Bosons, known as Nambu-Anderson-Goldstone-Higgs modes[4, 8–10], which recover the broken symmetry by using the phase degree of freedom, $\Delta = |\Delta|\mathrm{e}^{i\phi}$, in low energy excitation to circulate around the minimum of Ginzburg-Laudau free energy with the shape of a Mexican hat[11–13]. These theories[4, 8–10] saved the apparent contradiction of the variational BCS wavefunction[3, 4, 6] with the unfixed number of electrons, regardless of the definite number of electrons in a material, because the inclusion of the collective modes ensures the conservation law of charge under the current flow as a vertex correction of the Ward-Takahashi identity[4, 8]. It is also interesting to note that a fully analytic exact solution of a superconducting ground state with a fixed number of electrons, describing the vacuum state of collective modes, beyond the BCS wavefunction is still unknown even for a simplified BCS Hamiltonian. Nevertheless, the essential mechanism of superconductivity is considered to be understood based on the BCS theory. This statement would be mostly true even after the discoveries of new superconducting materials[14–17], including copper-oxides with d-wave paring symmetries[14, 18], although the source of the attractive interaction would be required to be reconsidered from phonon-mediated mechanism to spin-correlated one. It is considered that the normal states of the copper-oxides[18, 19] are even more anomalous than the superconducting states, since the strong Coulomb repulsion in two-dimensional ($2D$) leads the Mott-Hubbard metal-insulator transition and the validity of the Fermi liquid theory is marginal[11, 12, 18]. It is certainly beyond the authors abilities to grasp the entire recent progress on superconductivity. The subject of superconductivity is huge and still expanding significantly across interdisciplinary areas, and superconductivity is deeply linked to the forefront of fundamental physics on broken symmetries and the emergence of mass.

The effective mass[20–22] in a material is also very important for various practical electronic applications, especially for Metal-Oxide-Semiconductor (MOS) Field-Effect-Transistors (FETs), because the mobility is larger if the mass is smaller[20, 22–25] suitable for high speed operations. Novel strain-engineering technologies[25–27] are introduced in Si MOFETs to reduce the effective mass. Graphene[28–32] is especially promising for high-speed RF applications in this sense, because the effective mass vanishes at the $2D$ Dirac point[29, 33]. The band structure of the Graphene[34] was known for a long time, however, it was not considered to be able to isolate as a complete $2D$ layer, because the long-range order is not expected to realise at any finite

temperature due to thermal and quantum fluctuations[35–37]. It was a great discovery that the Graphene monolayer was exfoliated by a sticky tape[30, 31], which was a modern innovation like an Egg of Columbus. It is now considered that the ripples of Graphene are ensuring to stabilise its $2D$ crystalline structure without violating Mermin-Wagner's theorem[35–37]. Again, the dimensionality and the symmetry are closely linked to the massless character of Dirac Fermions[29, 33]. These Dirac Fermions can be considered to be generated from magnetic monopoloes located at the Dirac points[29, 38, 39], which are topologically protected due to the conservation of geometrical Pancharatnam-Berry phase factors[40, 41]. Thus, the features of Dirac Fermions are robust against perturbations, if the external fields are conserving space and time reversal symmetries and the state is continuously changing without an occurrence of a phase transition, including superconductivity, which leads to the emergence of mass in quasi-particles, as outlined above[4, 8]. The idea of exfoliation and its transfer was successfully expanded to wider materials beyond Graphene with multi-layered structures weakly stacked via van-der Walls force[42, 43]. This will allow us to create a completely new material with various combinations of stacked layers, which was not possible to fabricate based on conventional superlattice fabricated by traditional epitaxial growth technologies, so that $2D$ materials are revolutionising material science and technologies.

We have recently proposed a new family of carbon allotropes with topologically non-trivial structures[44]. Topology is a mathematical concept to distinguish an isolated ring from a linked chain, for example, and it allows us to classify structures by continuous deformation of a structure. From topological points of views, Graphene with ripples is obviously equivalent to that without a ripple, and stacked $2D$ materials are categorised as topologically trivial, which means there is neither a link nor a knot. On the the other hand, we can consider various topologically nontrivial structures with links and knots in carbon allotropes[44], which include Hopf-link[45], Whitehead-link, Trefoil-knots, Mebius ring, Bborromean rings, and so on. In particular, we think Hopf-links are very useful to extend the topologically non-trivial network in the form of a chain ($1D$), a chainmail ($2D$), and a crystal ($3D$). The Hopf-links can change spacial configuration without topologically changing the structure, so that it is strong against deformation. A Hopf-linked Carbon-Nano-Chain (CNC) can be stretched to change its length orders of magnitude, depending on whether it is relaxed or tensile-strained, similar to a macroscopic chain. The CNC does not have to maintain the rigid crystalline structure like a conventional crystal, while the topological feature is maintained as far as strong σ bonds are preserved, so that we can consider that the CNC possesses a topological-long-range order[44, 46–53]. By making arrays of Hopf-links, we can consider a new $3D$ crystalline carbon-allotrope, which links horizontal Graphene layers with vertical Graphene layers (Fig. 1). We have named this Hopf-linked Graphene layers as Hopfene, and the details of the structures are shown in Ref. [44]. Hopfene is classified by the way to insert Graphene layers against available slots, and $(1, 1)$-Hopfene is the most closely packed structure with AB-stacks between adjacent layers, while $(2, 2)$-Hopfene is made by AA-stacking with every other slot empty[44]. The crystal is tetragonal and

the lattice constants are $a = 3a_0$, $b = 3a_0 = a$, and $c = \sqrt{3}a_0$ with the bond length of carbon atoms a_0[44]. We have found that massless Dirac and Weyl Fermions exist in Hopfene and the observed flat-band features would be favourable for the appearance of superconductivity and other magnetic orders[54, 55].

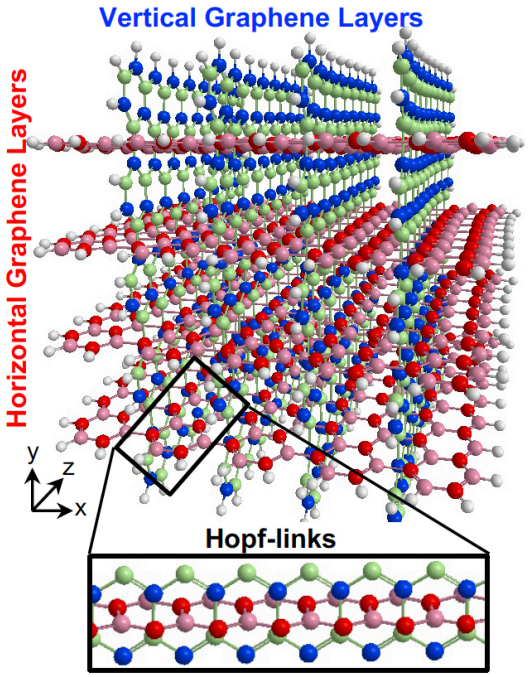

Figure 1. Hopf-linked Graphene layers: Hopfene. Graphene layers are linked both horizontally and vertically through Hopf-links without forming σ bonds between layers. Colours of carbon atoms are just guide to the eyes, representing A, B, C, and D-sublattices.

In this paper, we theoretically discuss superconductivity in (2,2)-Hopfene for the future, since various carbon allotropes exhibit superconductivity such as intercalated graphites[56, 57], K_3C_{60}[15], carbon-nano-tube[58, 59], Q-Carbon[16], and twisted bilayer Graphene[60]. In particular, we discuss the notion of the crossover[61–63] and possible quantum phase transitions[19, 64] from weak coupling BCS limit to strong coupling Bose-Einstein Condensation (BEC) of preformed pairs in Hopfene, because the attractive interaction is not know *a priori*, so that it is reasonable to assume the interaction strength as a free theoretical parameter. According to the conventional wisdom[61, 62], the evolution from BCS to BEC is rather continuous upon hypothetical increase of the attractive interaction strength, while the pictures are completely different between weak coupling Cooper paring in momentum space and strong coupling BEC of bipolarons in the real space[61, 62]. The formation of pre-formed pairs[65] might also be relevant to the pseudo-gap phenomena found in copper-oxides[18, 65] or excitonic condensation in graphite under high magnetic fields at the quantum limit[66]. More recently, it was theoretically identified that there exists a quantum critical point[19, 67–70] in $2D$ Graphene, so that the impact of vanishing

the Density-Of-State (DOS) at the Dirac points is significant on superconductivity[67–69]. The requirement of the finite critical attractive interaction strength at half-filling is a significant deviation from the BCS picture, which predicted the superconducting instability at the infinitely weak attractive interaction, while the BCS theory is still valuable to explain the superconductivity[68]. Our motivation of this study is to explore how the topological feature of the complicated band structure of Hopfene affects the BCS-BEC evolution scenario. We found non-trivial competitions between the formations of the semiconductor band gap and the superconducting gap near the quarterly fillings, where the superconducting order parameter is severely reduced and the system is close to a quantum critical point, where the superconducting transition temperature is reduced to be zero.

2. Model

2.1. Attractive Hubbard Model

We employ the attractive Hubbard Hamiltonian[61]

$$\hat{H} = -\sum_{ij\sigma} t_{ij}\hat{\psi}^{\dagger}_{i\sigma}\hat{\psi}_{j\sigma} - \mu\sum_{i\sigma}\hat{n}_{i\sigma} - U\sum_{i}\hat{n}_{i\uparrow}\hat{n}_{i\downarrow}, \tag{1}$$

where $\hat{\psi}^{\dagger}_{i\sigma}$ and $\hat{\psi}_{i\sigma}$ are creation and annihilation operators at the atomic lattice site i for spin σ, respectively, t_{ij} is the transfer energy between the lattice sites i and j, μ is chemical potential, $\hat{n}_{i\sigma}$ is the number operator, and U is the attractive interaction strength. In this paper, we focus on (2,2)-Hopfene (Fig. 1) and restrict the electron transfers within the nearest neighbour sites[44, 54]. In (2,2)-Hopfene, the numbers of sub-lattice atoms for all sublattices are the same $\mathcal{N} = \mathcal{N}_{\rm A} = \mathcal{N}_{\rm B} = \mathcal{N}_{\rm C} = \mathcal{N}_{\rm D}$, so that it is convenient to split the sum over all lattice sites into the sum within sub-lattices as

$$\sum_{i} = \sum_{\rm S=A,B,C,D}\sum_{i\in{\rm S}}^{\mathcal{N}}. \tag{2}$$

This means that we can assign a number from 1 to $\mathcal{N}$ for each atom with a sublattice index from A to D to describe the lattice coordinate of an atom. The total number of lattice sites is $\mathcal{N}_{\rm tot} = 4\mathcal{N} = 8\mathcal{N}_{\rm U}$ with the total number of the unit cell, $\mathcal{N}_{\rm U}$, and the number of sub-lattice atoms for each sublattice in the unit cell is 2 and the total number of atoms in the unit cell is 8. Similarly, it is convenient to describe $\hat{\psi}_{i\sigma}$ with a sublattice index as $\hat{\psi}_{i\sigma} = \hat{\psi}^{\rm S}_{i\sigma}$, and consequently we can define Fourier transformation and its inverse as

$$\hat{\psi}^{\rm S}_{\mathbf{k}\sigma} = \frac{1}{\sqrt{\mathcal{N}}}\sum_{i\in{\rm S}}^{\mathcal{N}}\hat{\psi}^{\rm S}_{i\sigma}{\rm e}^{-i\mathbf{k}\cdot\mathbf{x}_i} \tag{3}$$

$$\hat{\psi}^{\rm S}_{i\sigma} = \frac{1}{\sqrt{\mathcal{N}}}\sum_{\mathbf{k}}^{\mathcal{N}}\hat{\psi}^{\rm S}_{\mathbf{k}\sigma}{\rm e}^{i\mathbf{k}\cdot\mathbf{x}_i}, \tag{4}$$

respectively. We will describe the wave number vectors, $\mathbf{k}$, equivalent to the momentum $\mathbf{p} = \hbar\mathbf{k}$, in the unit of $2\pi(a^{-1}, a^{-1}, c^{-1})$ and $\hbar$ is the Dirac constant, which is the Plank constant divided by 2π.

Alternatively, we can also define the field-vector operator, $\hat{\boldsymbol{\psi}}_{i\sigma}$, with a sub-lattice index similar to a spinor description as $\hat{\boldsymbol{\psi}}_{i\sigma} = \left(\hat{\psi}^{\mathrm{A}}_{i\sigma}, \hat{\psi}^{\mathrm{B}}_{i\sigma}, \hat{\psi}^{\mathrm{C}}_{i\sigma}, \hat{\psi}^{\mathrm{D}}_{i\sigma}\right) = (a_{i\sigma}, b_{i\sigma}, c_{i\sigma}, d_{i\sigma})$, and its Fourier transform is $\hat{\boldsymbol{\psi}}_{\mathbf{k}\sigma} = (a_{\mathbf{k}\sigma}, b_{\mathbf{k}\sigma}, c_{\mathbf{k}\sigma}, d_{\mathbf{k}\sigma})$. This simplification was possible because of the same number of lattice sites among sub-lattices. If this was not the case, it is required to define two coordination vectors: one for the unit cell and the other for the relative vectors inside the cell.

Below, we will examine the 1st term of $\hat{H}$ as the kinetic energy Hamiltonian $\hat{H}_{\mathrm{kin}}$, the 2nd term as the chemical potential Hamiltonian $\hat{H}_{\mathrm{chem}}$, and the last term as the interaction Hamiltonian $\hat{H}_{\mathrm{int}}$ in more details.

2.2. Tight-Binding Hamiltonian

$\hat{H}_{\mathrm{kin}}$ represents delocalised π-electrons in the carbon network, and we expect 1 electron per atom without doping. The other 3 electrons among 4 electrons in the outer shell of a carbon atom are forming strong σ bonds. We assume the nearest neighbour transfer energy of $-t$ within Graphene layers and that of $-t_{\mathrm{H}}$ for Hopf-links. Then, we obtain

$$\hat{H}_{\mathrm{kin}} = \sum_{\mathbf{k}\sigma} \hat{\boldsymbol{\psi}}^{\dagger}_{\mathbf{k}\sigma} \begin{pmatrix} 0 & h_{\mathrm{AB}} & h_{\mathrm{AC}} & h_{\mathrm{AD}} \\ h^{*}_{\mathrm{AB}} & 0 & h_{\mathrm{BC}} & h_{\mathrm{BD}} \\ h^{*}_{\mathrm{AC}} & h^{*}_{\mathrm{BC}} & 0 & h_{\mathrm{CD}} \\ h^{*}_{\mathrm{AD}} & h^{*}_{\mathrm{BD}} & h^{*}_{\mathrm{CD}} & 0 \end{pmatrix} \hat{\boldsymbol{\psi}}_{\mathbf{k}\sigma}, \tag{5}$$

where we have defined

$$\begin{aligned}
h_{\mathrm{AB}} &= -t(\mathrm{e}^{ik_x a/3} + 2\mathrm{e}^{-ik_x a/6}\cos(k_z c/2)), \\
h_{\mathrm{CD}} &= -t(\mathrm{e}^{ik_y a/3} + 2\mathrm{e}^{-ik_y a/6}\cos(k_z c/2)), \\
h_{\mathrm{AC}} &= -t_{\mathrm{H}}(\mathrm{e}^{ik_x a/6}\mathrm{e}^{ik_y a/3} + \mathrm{e}^{-ik_x a/3}\mathrm{e}^{-ik_y a/6} + 2\mathrm{e}^{ik_x a/6}\mathrm{e}^{-ik_y a/6}\cos(k_z c/2)), \\
h_{\mathrm{AD}} &= -t_{\mathrm{H}}(\mathrm{e}^{ik_x a/6}\mathrm{e}^{-ik_y a/3} + \mathrm{e}^{-ik_x a/3}\mathrm{e}^{ik_y a/6} + 2\mathrm{e}^{ik_x a/6}\mathrm{e}^{ik_y a/6}\cos(k_z c/2)), \\
h_{\mathrm{BC}} &= -t_{\mathrm{H}}(\mathrm{e}^{-ik_x a/6}\mathrm{e}^{ik_y a/3} + \mathrm{e}^{ik_x a/3}\mathrm{e}^{-ik_y a/6} + 2\mathrm{e}^{-ik_x a/6}\mathrm{e}^{-ik_y a/6}\cos(k_z c/2)), \\
h_{\mathrm{BD}} &= -t_{\mathrm{H}}(\mathrm{e}^{-ik_x a/6}\mathrm{e}^{-ik_y a/3} + \mathrm{e}^{ik_x a/3}\mathrm{e}^{ik_y a/6} + 2\mathrm{e}^{-ik_x a/6}\mathrm{e}^{ik_y a/6}\cos(k_z c/2)).
\end{aligned}$$

If we define the Hamiltonian matrix for Graphene as

$$\mathcal{H}_{\mathrm{G}}(h) = \begin{pmatrix} 0 & h \\ h^{*} & 0 \end{pmatrix},$$

and that of Hopf-links as

$$h_{\mathrm{H}} = \begin{pmatrix} h_{\mathrm{AC}} & h_{\mathrm{AD}} \\ h_{\mathrm{BC}} & h_{\mathrm{BD}} \end{pmatrix},$$

then, it can be summarised as

$$\hat{H}_{\mathrm{kin}} = \sum_{\mathbf{k}\sigma} \hat{\boldsymbol{\psi}}^{\dagger}_{\mathbf{k}\sigma} \begin{pmatrix} \mathcal{H}_{\mathrm{G}}(h^{\mathrm{AB}}) & \mathcal{H}_{\mathrm{H}} \\ \mathcal{H}^{*}_{\mathrm{H}} & \mathcal{H}_{\mathrm{G}}(h^{\mathrm{CD}}) \end{pmatrix} \hat{\boldsymbol{\psi}}_{\mathbf{k}\sigma}. \tag{6}$$

In the limit of the absence of the Hopf-link transfer, $t_{\rm H} \to 0$, the energy dispersion reduces to that of Graphene for Dirac Fermions

$$\epsilon_{\rm AB}(\mathbf{k}) = \pm\sqrt{|h_{\rm AB}|^2} = \pm\sqrt{1+4\cos^2(k_z c/2)+4\cos(k_x a/2)\cos(k_z c/2)} \quad (7)$$

$$\epsilon_{\rm CD}(\mathbf{k}) = \pm\sqrt{|h_{\rm CD}|^2} = \pm\sqrt{1+4\cos^2(k_z c/2)+4\cos(k_y a/2)\cos(k_z c/2)}, \quad (8)$$

with $t = 2.8$ eV [29, 33, 34]. In general, $t_{\rm H} \neq 0$, we need to diagonalise $\hat{H}_{\rm kin}$ numerically at each $\mathbf{k}$, and we can obtain the band diagram with 4 energy dispersions, $\epsilon_1(\mathbf{k}) - \epsilon_4(\mathbf{k})$, labelled from the bottom. After the diagonalisation, the state will carry the band index, α, instead of S, and we obtain

$$\hat{H}_{\rm kin} = \sum_{\mathbf{k}\sigma\alpha} \epsilon_\alpha \hat{\psi}^\dagger_{\mathbf{k}\sigma\alpha}\hat{\psi}_{\mathbf{k}\sigma\alpha}. \quad (9)$$

Figure 2 shows examples of calculated tight-binding band structures. At $t_{\rm H} = 0$, electrons in Graphene layers cannot transfer from each other through Hopf-links, so that electrons are confined within Garphene layers. In this case, the band dispersions are flat against the directions perpendicular to the Graphene layers, so that we have flat-bands along k_x, from $(0, 0.5, 1)$ to $(0.5, 0.5, 1)$, and k_y, from $(0, 0, 1)$ to $(0, 0.5, 1)$ (Fig. 2 (a)). There are 10 Dirac points at $(\pm 1, 0, \pm 1/3)$, $(0, \pm 1, \pm 1/3)$, and $(0, 0, \pm 2/3)$. Among these points, at $(0, 0, \pm 2/3)$, Dirac points coming from horizontal and vertical Graphene layers are degenerate (Fig. 2 (a)). Therefore, we can recognise 2 dispersion curves are completely overlapping around the Dirac point (Fig. 2 (a)). At $t_{\rm H} \neq 0$, Dirac point at $(0, 0, 2/3)$ split into 2 Dirac points (Figs. 2 (b) and (c)) due to the formation of bonding and anti-bonding states through Hopf-links. We have compared these tight-binding results with the first-principle calculations[55] and confirmed reasonable agreements and extracted $t_{\rm H} = 1.5$ eV. All calculations below are based on this parameter with $t = 2.8$ eV [29, 33, 34] and $t_{\rm H} = 1.5$ eV.

2.3. Dirac points and nodal lines

Due to its analytic nature of the tight-binding model, it is easy to calculate energy band dispersions, $\epsilon_\alpha = \epsilon_\alpha(k_x, k_y, k_z)$. However, we must fix 1 component in order to describe in a $3D$ form (Fig. 3). We can recognise Dirac points in the (k_x, k_z) plot at fixed $k_y = 0$ (Fig. 3 (a)), and the dispersion is symmetric under the exchange of k_x and k_y, so that exactly the same energy dispersion is obtained in the (k_y, k_z) plot at $k_x = 0$ (not shown). At $k_z = 0$, we do not see Dirac points, and a simple band interception was found at the zone edge of $(1, 1, 0)$. We also found the broken particle-hole symmetry, which means $\epsilon_\alpha(k_x, k_y, k_z)$ is symmetric against $\epsilon = 0$ by the change of the sign. The particle-hole symmetries were found in Graphene layers, as seen in $\epsilon_{\rm AB}$ and $\epsilon_{\rm CD}$ of Eqs. (7) and (8), while it was broken at $t_{\rm H} \neq 0$. This could be understood simply by diagonalising 2 and 3 sites models as shown in Table 1. The simplest 2 sites model will give two energy states, corresponding to particle and hole state with the energy of t and $-t$, respectively. If we introduce 1 more site allowing equivalent transfers to these 2 sites, mimicking Hopf-links, we obtain the asymmetric eigenstates, $-t - 2t_{\rm H}^2/t$, $2t_{\rm H}^2/t$, and t, in

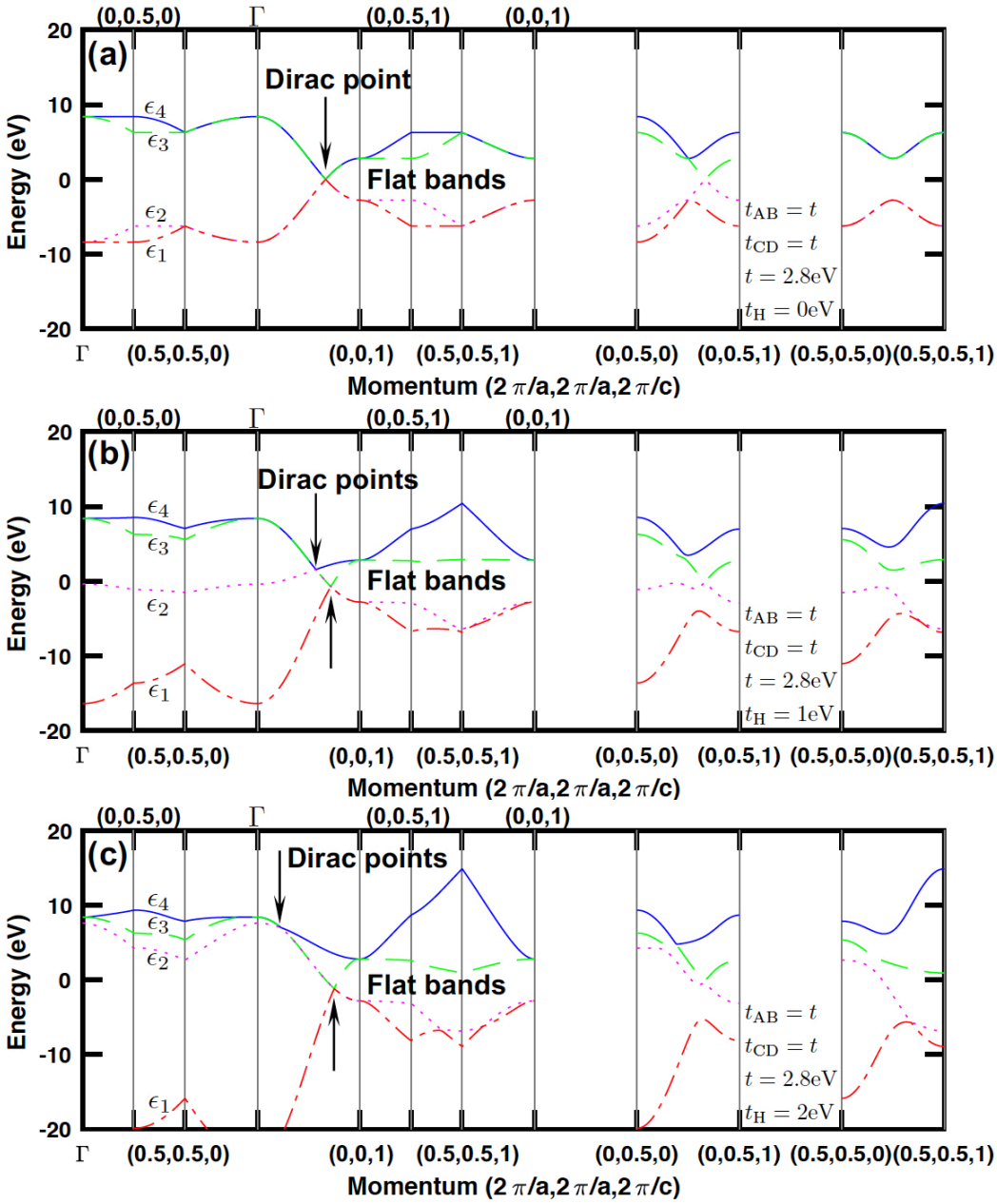

Figure 2. Tight-binding band structures of (2,2)-Hopfene at (a)$t_H = 0$, (b) $t_H = 1$ eV, and (c) $t_H = 2$ eV. The original Dirac point at (0,0,2/3) was degenerate at $t_H = 0$, and it splits into 2 Dirac points with the introduction of $t_H \neq 0$ due to the hybridisation. Flat-bands also exist due to the original $2D$ character of Graphene, showing weak dispersion along the directions perpendicular to the Graphene layers, which remained with $t_H \neq 0$.

the limit of $t \gg t_H$. Therefore, the energy levels depend on the sign of t and the particle-hole symmetry is broken. On the other hand, the sign change of t_H does not break the particle-hole symmetry. This comes from the fact that 2 transfers through Hopf-link are required to come back to the original Graphene sites, so that the sign change of

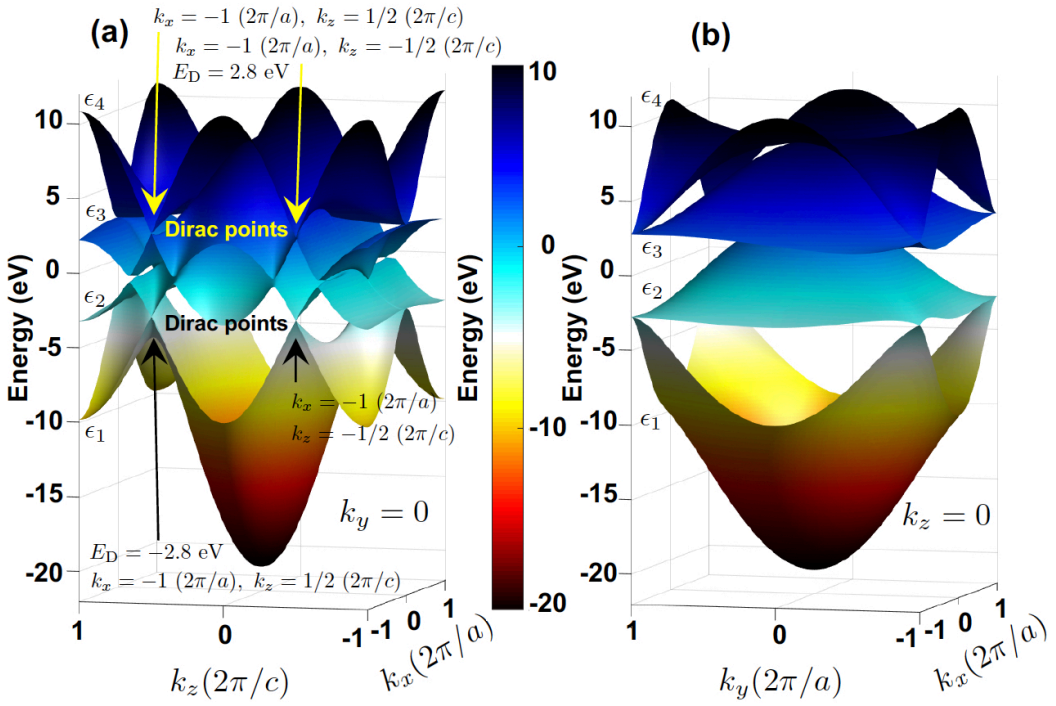

Figure 3. Bend structures of (2,2)-Hopfene at (a) $k_y = 0$ and (b) $k_z = 0$, calculated at $t_{\rm H} = 1.5$ eV.

Table 1. Two and three sites models for the impacts of signs in transfer energies

Model	Hamiltonian	Eigenvalues	Eigenvalues ($t \gg t_{\rm H}$)
2 sites	$\begin{pmatrix} 0 & -t \\ -t & 0 \end{pmatrix}$	$\pm t$	$\pm t$
2 sites + Hopf-link	$\begin{pmatrix} 0 & -t & -t_{\rm H} \\ -t & 0 & -t_{\rm H} \\ -t_{\rm H} & -t_{\rm H} & 0 \end{pmatrix}$	t,$-\frac{1}{2}\left(t \pm \sqrt{t^2+8t_{\rm H}^2}\right)$	$-t-\frac{2t_{\rm H}^2}{t}, \frac{2t_{\rm H}^2}{t}, t$
Negative transfer	$\begin{pmatrix} 0 & -t & -t_{\rm H} \\ t & 0 & -t_{\rm H} \\ t_{\rm H} & -t_{\rm H} & 0 \end{pmatrix}$	-t,$\frac{1}{2}\left(t \pm \sqrt{t^2+8t_{\rm H}^2}\right)$	$-t, -\frac{2t_{\rm H}^2}{t}, t+\frac{2t_{\rm H}^2}{t}$
Negative Hopf-link	$\begin{pmatrix} 0 & -t & t_{\rm H} \\ -t & 0 & t_{\rm H} \\ t_{\rm H} & t_{\rm H} & 0 \end{pmatrix}$	t,$-\frac{1}{2}\left(t \pm \sqrt{t^2+8t_{\rm H}^2}\right)$	$-t-\frac{2t_{\rm H}^2}{t}, \frac{2t_{\rm H}^2}{t}, t$

$t_{\rm H}$ cannot contribute. More generally in Hopfene, even number of transfers thorough Hopf-links are required to come back, so that the obtained energy bands $\epsilon_\alpha(k_x, k_y, k_z)$ did not change by $t_{\rm H} \to -t_{\rm H}$. Please also note that the spacial reflection symmetry $\mathbf{k} \to -\mathbf{k}$ ($\epsilon_\alpha(\mathbf{k}) = \epsilon_\alpha(-\mathbf{k})$) and the time reversal symmetry $t \to -t$ are still maintained without applying magnetic fields. It is also symmetric with the exchange of k_x and k_y in $(2,2)$-Hopfene, due to the symmetry between horizontal and vertical directions, but it would not be the case in (n,m)-Hopfene with $n \neq m$.

Another interesting feature of the band diagram of Hopfene is the existence of nodal

lines[39] (Fig. 4). This is coming from the original flat dispersion relationships of $\epsilon_{\rm AB}$ and $\epsilon_{\rm CD}$ against k_y and k_x, which are directions perpendicular to horizontal AB-layers and vertical CD-layers, respectively. Therefore, the bands close to the Dirac points are also dispersionless along these directions, so that Dirac points are connected as nodal lines. Once nodal lines were formed, they cannot be eliminated upon the adiabatic introduction of $t_{\rm H}$, since nodal lines are topologically protected. In the example of Fig. 3, nodal lines have dispersion along $k_x = k_y - 1$ at $k_z = 1/2$ but the lines are in perfect agreement with the adjacent bands (Fig. 3 (b)), confirming the degeneracies and topological features of band diagrams.

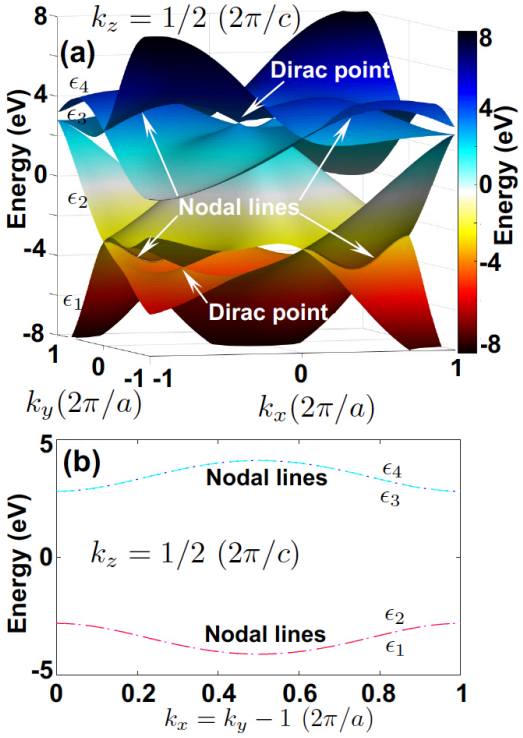

Figure 4. Dirac points and nodal lines at $k_z = 1/2$. (a) Energy dispersions along k_x and k_y. (b) Energy dispersions along $k_x = k_y - 1$ to show the nodal lines. ϵ_4 (dotted blue) and ϵ_3 (dashed cyan) are completely overlapping, and ϵ_2 (dotted magenta) and ϵ_1 (dashed red) are also overlapping.

2.4. Fermi surface

In the presence of $t_{\rm H}$, electronic states between horizontal and vertical Graphene layers are hybridised to form topologically unique Fermi surfaces[54]. The band structures can be highlighted by the existence of $3D$, $2D$, and $1D$ Weyl and Dirac Fermions[54] with flat-band features (Fig. 2). The Fermi energy of the non-doped (2,2)-Hopfene was $E_{\rm F} = 1.1$ eV, but this could be changed by doping alkali-atoms[15, 56, 57] or NH_3[71] at interstitial sites due to the large spacing in the unit cell[44, 54]. Here, we describe typical structures of Fermi surfaces in (2,2)-Hopfene.

$3D$ Weyl Fermions exist around at the Dirac point with the energy of $E_{\rm d} = -1.0$ eV, where ϵ_3 and ϵ_2 have linear dispersions along all 3 directions, k_x, k_y, and k_z, and therefore, the spatial quantum confinements are strongest[54]. Figure 5 shows the Fermi surface of $3D$ Weyl Fermions below ($E_{\rm F} = -0.8$ eV, Figs 5 (a) and (c)) and above ($E_{\rm F} = -1.2$ eV, Figs 5 (b) and (d)) this point at $E_{\rm d} = -1.0$ eV. Fermi surfaces of $3D$ Weyl Fermions are small, because of the limited DOS due to strong confinements and linear dispersions. The reduced DOS is not favourable for superconductivity[67–70], as we shall see in the following sections for Hopfene. The Fermi surface of ϵ_1 in Fig. 5 (d) is particularly unique, because the 2 edges of the Fermi surface are connected to the Fermi surfaces of ϵ_2 by point-contacts. This is originated from the nodal lines, shown in Fig. 4. Due to the close proximity of the Dirac point to the nodal lines, the Fermi surfaces of ϵ_1 were terminated on the nodal lines, so that Fermi surfaces of ϵ_1 and ϵ_2 were connected by points without overlapping each other. This topological feature is maintained to a certain extent, and the filling of these bands were competing: as we increase $E_{\rm F}$, ϵ_1 is eventually occupied completely, leading to the reduction of the size of the Fermi surface of lower valley (Fig. 5 (d)) for $3D$ Weyl Fermions, and the flat-bands of ϵ_2 is taking over the area, while further increase of $E_{\rm F}$ induces the reduction of the volume of Fermi surfaces of ϵ_2, and the Fermi surface of the upper valley (Fig. 5 (c)) starts to take over.

We also found the weaker confinements at the $1D$ Dirac point of $E_{\rm d} = 2.7$ eV, where the confinement is strong only along k_x direction (Fig. 6). The Fermi surfaces located these valleys are more spreading along vertical and diagonal directions, since band dispersions along these directions are flat (Figs. 6 (b) and (c)). We can also recognise that the close proximity of nodal lines near $E_{\rm d}$ due to the point contacts of the Fermi surfaces of ϵ_4 with ϵ_3, at (0,0,1), which is equivalent to (0,0,-1).

A similar point-contacts of the Fermi surfaces were also found at $E_{\rm d} = -4.3$ eV (Fig. 7), where 4 Dirac points are found and each Fermi surface of the upper valleys (ϵ_2) have 4 point contacts to the Fermi surfaces of the lower band (ϵ_1). As we increase $E_{\rm F}$, the flat-bands of ϵ_1 (Fig. 7 (a)) are gradually filled, leading to the reduced Fermi surfaces, and eventually the Fermi surfaces of another flat-bands of ϵ_2 (Fig. 7 (b)) start to grow. These changes of the Fermi surfaces upon increasing $E_{\rm F}$ will give important consequences on the evolutions of superconductivity using these valleys, and the larger DOS is favourable for larger superconducting order parameters, as expected from the BCS theory[3, 4, 6, 61, 62].

2.5. Density of states

The DOS per unit volume per spin for the band α is given by

$$D^{\alpha}_{V\sigma}(\epsilon) = \frac{1}{V}\sum_{\mathbf{k}} \delta\left(\epsilon - \epsilon^{\alpha}(\mathbf{k})\right) \tag{10}$$

$$= \frac{2}{v_{\rm U}} \int_{-1/2}^{1/2} dk_x \int_{-1/2}^{1/2} dk_y \int_{-1/2}^{1/2} dk_z \delta\left(\epsilon - \epsilon^{\alpha}(\mathbf{k})\right) \tag{11}$$

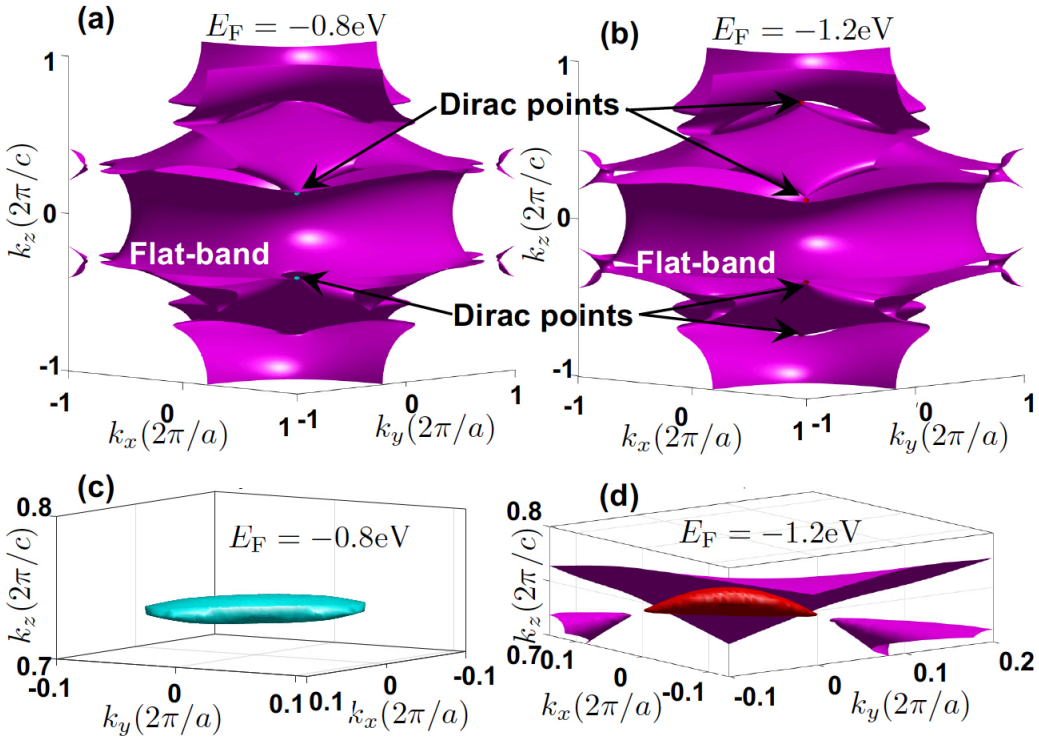

Figure 5. $3D$ Weyl Fermions in Hopfene. Fermi surfaces of the bands ϵ_3, ϵ_2, and ϵ_1 are shown in colours of cyan, magenta, and red, respectively. Fermi surfaces at (a) $E_F = -0.8$ eV and (b) $E_F = -1.2$ eV. Flat-bands if ϵ_2 were dominated, while the small Fermi surfaces for $3D$ Weyl Fermions are found around edges. $3D$ Weyl Fermions in (c) upper valleys at $E_F = -0.8$ eV and (d) lower valley at $E_F = -1.2$ eV.

$$= \frac{2}{v_U}\int_{-1}^{1}\frac{dk_x}{2}\int_{-1}^{1}\frac{dk_y}{2}\int_{-1}^{1}\frac{dk_z}{2}\delta\left(\epsilon-\epsilon^{\alpha}(\mathbf{k})\right), \tag{12}$$

where V is the volume of the system, $v_U = abc$ is the volume of the unit cell, a factor of 2 in Eq. (11) is coming from the number of each sub-lattice atoms in the unit cell, and Eq. (12) is described by the integration in the extended Brillouin zone of $k_x \in (-2\pi/a, 2\pi/a)$, $k_y \in (-2\pi/a, 2\pi/a)$, and $k_z \in (-2\pi/c, 2\pi/c)$. The DOS per unit cell per spin for the band α is

$$D^{\alpha}_{U\sigma}(\epsilon) = v_U D^{\alpha}_{V\sigma}(\epsilon). \tag{13}$$

The total number of atoms per unit cell is $4 \times 2 = 8$, so that the DOS per atom per spin for the band α is given by

$$D^{\alpha}_{0\sigma}(\epsilon) = \frac{1}{4}\int_{-1}^{1}\frac{dk_x}{2}\int_{-1}^{1}\frac{dk_y}{2}\int_{-1}^{1}\frac{dk_z}{2}\delta\left(\epsilon-\epsilon^{\alpha}(\mathbf{k})\right), \tag{14}$$

and the total DOS per atom per spin is

$$D_{0\sigma}(\epsilon) = \sum_{\alpha=1}^{4} D^{\alpha}_{0\sigma}(\epsilon), \tag{15}$$

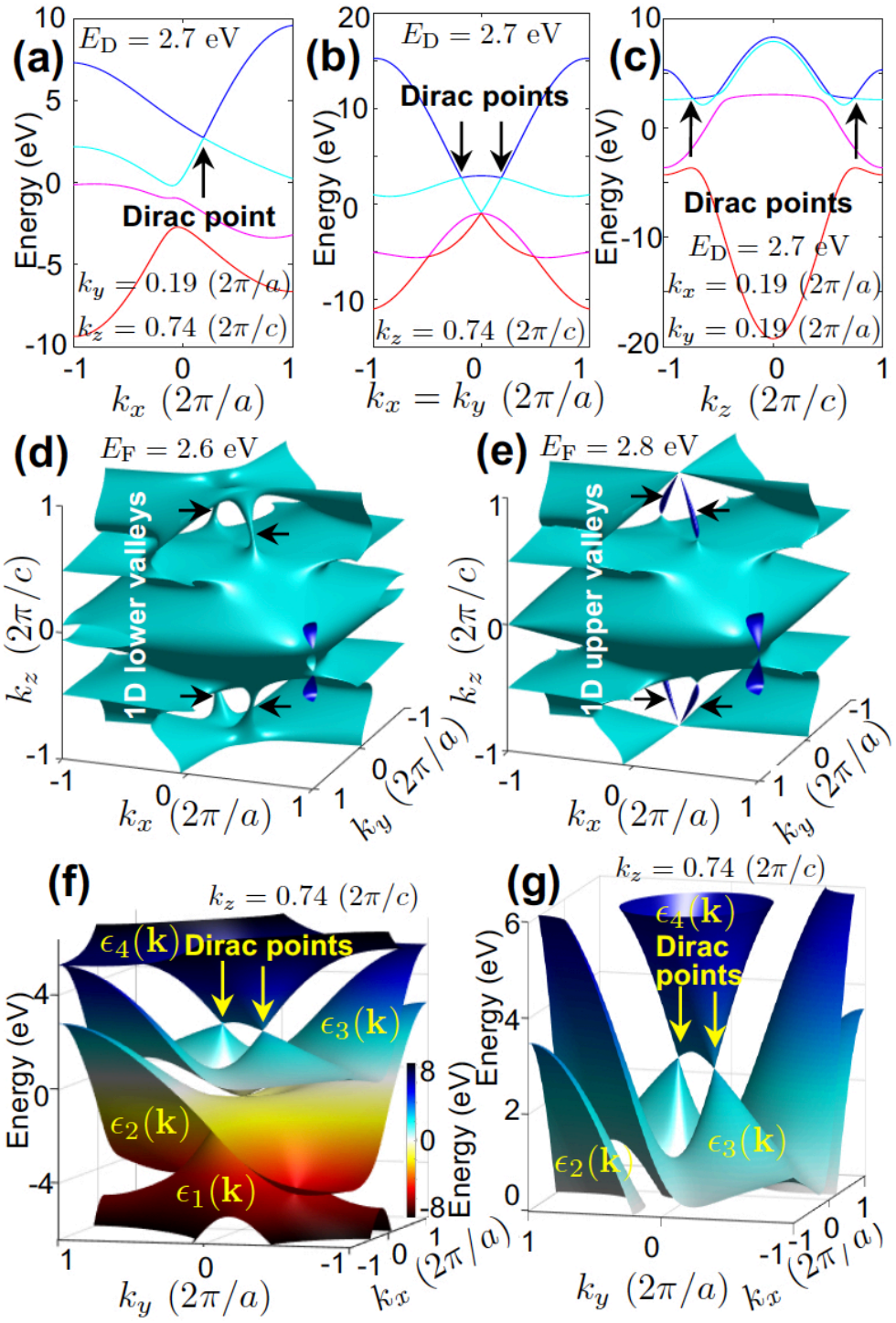

Figure 6. $1D$ Dirac Fermions at $(0.19, 0.19, 0.74)$. (a) Horizontal k_x at fixed $k_y = 0.19$ and $k_z = 0.74$, (b) diagonal $k_x = k_y$at fixed $k_z = 0.74$, and (c) vertical dependences of band dispersions. Fermi surfaces of (c) lower valley (ϵ_3, cyan) and (d) upper valley (ϵ_4, blue). Energy band structures at (f) $k_z = 0.74$ and (g) its extended view.

which satisfies the sum rule

$$\int_{-\infty}^{\infty} d\epsilon D_{0\sigma}(\epsilon) = \sum_{\alpha=1}^{4} \frac{1}{4} = 1, \tag{16}$$

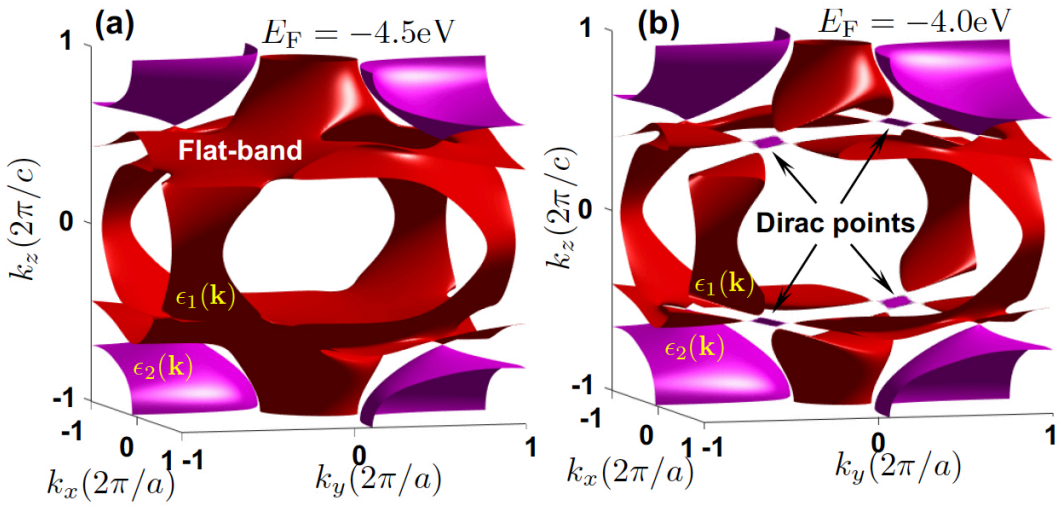

Figure 7. Flat-bands near Dirac points. Fermi surfaces for (a) lower valleys at $E_F = -4.5$ eV and (a) upper valleys at $E_F = -4.0$ eV.

meaning that each atom can accommodate 1 electron per spin, so that the maximum number of 2 electrons can occupy an atom including spin.

Figure 8 shows the calculated DOS of non-interacting electrons at $t_H = 1.5$ eV. The band structure predicts semi-metal characteristics with peaks, coming from flat-bands. The point contact of ϵ_1 and ϵ_3 bands at $\epsilon = -1.0$ eV is showing $3D$ Dirac point, where the peak of DOS of the band ϵ_2 is coming from the flat-band feature (Fig. 5).

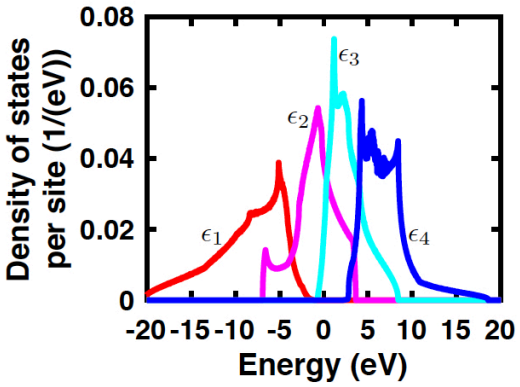

Figure 8. Density of states calculated for (2,2)-Hopfene at $t_H = 1.5$ eV.

2.6. Mean-field theory

Finally, we will focus on the impact of the attractive interaction Hamiltonian,

$$\hat{H}_{\rm int} = -U \sum_{\rm S=A,B,C,D} \sum_{i\in \rm S} \hat{n}^{\rm S}_{i\uparrow} \hat{n}^{\rm S}_{i\downarrow}, \tag{17}$$

where $\hat{n}^{\rm S}_{i\sigma}$ is the number operator at the site i in the sub-lattice S. We introduce Fourier transformation and its inverse of $\hat{n}^{\rm S}_{i\sigma}$ as

$$\hat{\rho}^{\rm S}_{\mathbf{q}\sigma} = \sum_{i\in {\rm S}}^{\mathcal{N}} \hat{n}^{\rm S}_{i\sigma} {\rm e}^{-i\mathbf{q}\cdot\mathbf{x}_i} = \sum_{\mathbf{k}} \hat{\psi}^{\rm S\dagger}_{\mathbf{k}\sigma}\hat{\psi}^{\rm S}_{\mathbf{k}+\mathbf{q}\sigma} \tag{18}$$

$$\hat{n}^{\rm S}_{i\sigma} = \frac{1}{\mathcal{N}}\sum_{\mathbf{q}} \hat{\rho}^{\rm S}_{\mathbf{q}\sigma}{\rm e}^{i\mathbf{q}\cdot\mathbf{x}_i}. \tag{19}$$

Inserting these into $\hat{H}_{\rm int}$, we obtain

$$\hat{H}_{\rm int} = -\frac{U}{\mathcal{N}} \sum_{\rm S=A,B,C,D} \sum_{i\in {\rm S}} \hat{\rho}^{\rm S}_{\mathbf{q}\uparrow}\hat{\rho}^{\rm S}_{-\mathbf{q}\downarrow}, \tag{20}$$

which shows the interaction works within the sub-lattice, because of the local nature of the Hubbard interaction. We examine how the interaction works among sub-bands after the diagonalisation of the kinetic Hamiltonian as

$$\hat{H}_{\rm kin} = \sum_{\rm S,S'}\sum_{\mathbf{k},\sigma} \hat{\psi}^{\rm S}_{\mathbf{k}\sigma}\mathcal{H}^{\rm SS'}_{\rm kin}(\mathbf{k})\hat{\psi}^{\rm S'}_{\mathbf{k}\sigma} \tag{21}$$

$$= \sum_{\alpha}\sum_{\mathbf{k},\sigma} \hat{\psi}^{\alpha}_{\mathbf{k}\sigma}\mathcal{H}^{\alpha\alpha}_{\rm kin}(\mathbf{k})\hat{\psi}^{\alpha}_{\mathbf{k}\sigma}, \tag{22}$$

where the Hamiltonian matrix

$$\mathcal{H}^{\alpha\alpha'}_{\rm kin}(\mathbf{k}) = U^{\dagger}_{\alpha{\rm S}}(\mathbf{k})\mathcal{H}^{\rm SS'}_{\rm kin}(\mathbf{k})U_{{\rm S}'\alpha'}(\mathbf{k}) \tag{23}$$

$$= \epsilon_{\alpha}(\mathbf{k})\delta_{\alpha\alpha'}, \tag{24}$$

was diagonalised by the unitary matrix $U_{{\rm S}\alpha}$. It is not trivial whether the interaction is still within the intra-bands, because $U_{{\rm S}\alpha}$ is included in the Fourier transform of the density operator as

$$\hat{\rho}^{\rm S}_{\mathbf{q}\sigma} = \sum_{\mathbf{k}}\sum_{\alpha\alpha'} U^{*}_{{\rm S}\alpha}(\mathbf{k})U_{{\rm S}\alpha'}(\mathbf{k}+\mathbf{q})\hat{\psi}^{\alpha\dagger}_{\mathbf{k}\sigma}\hat{\psi}^{\alpha'}_{\mathbf{k}+\mathbf{q}\sigma}, \tag{25}$$

and we obtain

$$\begin{aligned}\hat{H}_{\rm int} = & -\frac{U}{\mathcal{N}}\sum_{\mathbf{k}\mathbf{k}'\mathbf{q}}\sum_{\rm S}\sum_{\alpha_1\alpha_2\alpha_3\alpha_4} \\ & U^{*}_{{\rm S}\alpha_1}(\mathbf{k})U^{*}_{{\rm S}\alpha_3}(-\mathbf{k}')U_{{\rm S}\alpha_4}(-(\mathbf{k}'+\mathbf{q}))U_{{\rm S}\alpha_2}(\mathbf{k}+\mathbf{q}) \\ & \hat{\psi}^{\alpha_1\dagger}_{\mathbf{k}\uparrow}\hat{\psi}^{\alpha_3\dagger}_{-\mathbf{k}'\downarrow}\hat{\psi}^{\alpha_4}_{-(\mathbf{k}'+\mathbf{q})\downarrow}\hat{\psi}^{\alpha_2}_{\mathbf{k}+\mathbf{q}\uparrow}.\end{aligned} \tag{26}$$

We show the products of unitary matrices do not contribute in the end. We utilise the fundamental character of the Unitary matrix, $U^{-1} = U^{\dagger}$, namely

$$\left(U^{-1}(\mathbf{k})\right)_{{\rm S}_1{\rm S}_2} = U^{*}_{{\rm S}_2{\rm S}_1}(\mathbf{k}), \tag{27}$$

and the reflection symmetry of the system

$$U_{{\rm S}_1{\rm S}_2}(-\mathbf{k}), = U^{*}_{{\rm S}_1{\rm S}_2}(\mathbf{k}). \tag{28}$$

In the Cooper channel, the contribution from the zero center-of-mass momentum of the Cooper pair dominates due to BEC nature of superconductivity, so that the pairing

of $\mathbf{k}' = \mathbf{k}$ within the sub-babnds in $\hat{H}_{\rm int}$ dominates. Then, we consider

$$\begin{aligned}\sum_{\alpha_1=\alpha_3} U^*_{{\rm S}\alpha_1}(\mathbf{k})U^*_{{\rm S}\alpha_3}(-\mathbf{k}) &= \sum_{\alpha_1} \left(U(\mathbf{k})^{-1}\right)_{\alpha_1{\rm S}} \left(U(\mathbf{k})\right)_{{\rm S}\alpha_1} \\ &= \left(U(\mathbf{k})U(\mathbf{k})^{-1}\right)_{\rm SS} \\ &= 1. \end{aligned} \tag{29}$$

Similarly, we confirm

$$\begin{aligned}\sum_{\alpha_4=\alpha_2} U^*_{{\rm S}\alpha_4}(-(\mathbf{k}+\mathbf{q}))U^*_{{\rm S}\alpha_2}(\mathbf{k}+\mathbf{q}) &= \sum_{\alpha_2} \left(U(\mathbf{k}+\mathbf{q})\right)_{{\rm S}\alpha_2} \left(U(\mathbf{k}+\mathbf{q})^{-1}\right)_{\alpha_2{\rm S}} \\ &= \left(U(\mathbf{k}+\mathbf{q})U(\mathbf{k}+\mathbf{q})^{-1}\right)_{\rm SS} \\ &= 1. \end{aligned} \tag{30}$$

Therefore, the dominant interaction would be the paring within sub-bands

$$\hat{H}_{\rm Cooper} = -\frac{U}{\mathcal{N}} \sum_{\mathbf{k}\mathbf{k}'} \sum_{\alpha} \hat{\psi}^{\alpha\dagger}_{\mathbf{k}\uparrow}\hat{\psi}^{\alpha\dagger}_{-\mathbf{k}\downarrow}\hat{\psi}^{\alpha}_{-\mathbf{k}'\downarrow}\hat{\psi}^{\alpha}_{\mathbf{k}'\uparrow}, \tag{31}$$

and the factor of unitary matrices become unity.

Another dominant source of interaction is the Hartree-Fock channel at $\mathbf{q} = 0$

$$\begin{aligned}\hat{H}_{\rm HF} = &-\frac{U}{\mathcal{N}} \sum_{\mathbf{k}\mathbf{k}'} \sum_{\rm S} \sum_{\alpha_1\alpha_2\alpha_3\alpha_4} \\ &U^*_{{\rm S}\alpha_1}(\mathbf{k})U_{{\rm S}\alpha_2}(\mathbf{k})U^*_{{\rm S}\alpha_3}(-\mathbf{k}')U_{{\rm S}\alpha_4}(-(\mathbf{k}')) \\ &\hat{\psi}^{\alpha_1\dagger}_{\mathbf{k}\uparrow}\hat{\psi}^{\alpha_2}_{\mathbf{k}\uparrow}\hat{\psi}^{\alpha_3\dagger}_{-\mathbf{k}'\downarrow}\hat{\psi}^{\alpha_4}_{-\mathbf{k}'\downarrow}, \end{aligned} \tag{32}$$

for which the main contribution is coming from the intra-band interaction to conserve the number of electrons in each sub-band. Then, we consider

$$\begin{aligned}\sum_{\alpha_1=\alpha_2} U^*_{{\rm S}\alpha_1}(\mathbf{k})U_{{\rm S}\alpha_2}(\mathbf{k}) &= \sum_{\alpha_1} \left(U(\mathbf{k})^{-1}\right)_{\alpha_1{\rm S}} \left(U(\mathbf{k})\right)_{{\rm S}\alpha_1} \\ &= \left(U(\mathbf{k})U(\mathbf{k})^{-1}\right)_{\rm SS} \\ &= 1. \end{aligned} \tag{33}$$

Similarly, we confirm

$$\begin{aligned}\sum_{\alpha_3=\alpha_4} U^*_{{\rm S}\alpha_3}(-\mathbf{k}')U_{{\rm S}\alpha_4}(-\mathbf{k}') &= \sum_{\alpha_3} \left(U(-\mathbf{k}')^{-1}\right)_{\alpha_3{\rm S}} \left(U(-\mathbf{k}')\right)_{{\rm S}\alpha_3} \\ &= \left(U(-\mathbf{k}')U(-\mathbf{k}')^{-1}\right)_{\rm SS} \\ &= 1. \end{aligned} \tag{34}$$

Therefore, we obtain

$$\hat{H}_{\rm HF} \approx -\frac{U}{\mathcal{N}} \sum_{\mathbf{k}\mathbf{k}'} \sum_{\alpha} \hat{\psi}^{\alpha\dagger}_{\mathbf{k}\uparrow}\hat{\psi}^{\alpha}_{\mathbf{k}\uparrow}\hat{\psi}^{\alpha\dagger}_{-\mathbf{k}'\downarrow}\hat{\psi}^{\alpha}_{-\mathbf{k}'\downarrow}, \tag{35}$$

and the unitary matrix $U_{{\rm S}\alpha}(\mathbf{k})$ does not contribute to expectation values.

The unitary transformation does not change the total number of electrons

$$\hat{N} = \sum_{\mathbf{k}\sigma{\rm S}} \hat{\psi}^{\rm S\dagger}_{\mathbf{k}\sigma}\hat{\psi}^{\rm S}_{\mathbf{k}\sigma} = \sum_{\mathbf{k}\sigma\alpha} \hat{\psi}^{\alpha\dagger}_{\mathbf{k}\sigma}\hat{\psi}^{\alpha}_{\mathbf{k}\sigma}, \tag{36}$$

either. We can also define the average number of electrons per atom for each sub-lattice

$$n_{\rm S} = \frac{1}{\mathcal{N}} \sum_{\mathbf{k}\sigma} \langle \hat{\psi}^{\rm S\dagger}_{\mathbf{k}\sigma} \hat{\psi}^{\rm S}_{\mathbf{k}\sigma} \rangle, \tag{37}$$

which is $n_{\rm S} \in (0, 2)$ and the filling fraction is defined by $n_{\rm S}/2 \in (0, 1)$. The average total number of electrons per site among all 4 sub-lattices is

$$n = \frac{1}{4} \sum_{\rm S=A,B,C,D} n_{\rm S}. \tag{38}$$

At zero temperature, $T = 0$, we use the BCS wavefunction[3, 4, 6, 7, 61]

$$|{\rm BCS}\rangle = \prod_{\mathbf{k}\alpha} \left[u^{\alpha}_{\mathbf{k}} + v^{\alpha}_{\mathbf{k}} \hat{\psi}^{\alpha\dagger}_{\mathbf{k}\uparrow} \hat{\psi}^{\alpha\dagger}_{-\mathbf{k}\downarrow} \right] |0\rangle, \tag{39}$$

where $u^{\alpha}_{\mathbf{k}}$ and $v^{\alpha}_{\mathbf{k}}$ are described as

$$u^{\alpha}_{\mathbf{k}} = \cos\left(\frac{\theta^{\alpha}_{\mathbf{k}}}{2}\right) \tag{40}$$

$$v^{\alpha}_{\mathbf{k}} = {\rm e}^{i\phi} \sin\left(\frac{\theta^{\alpha}_{\mathbf{k}}}{2}\right) \tag{41}$$

with the superconducting $U(1)$ phase, ϕ, to satisfy the normalisation condition

$$|u^{\alpha}_{\mathbf{k}}|^2 + |v^{\alpha}_{\mathbf{k}}|^2 = 1 \tag{42}$$

for $\langle {\rm BCS}|{\rm BCS}\rangle = 1$. Then, we can calculate the thermodynamic potential energy[3, 4, 6, 7, 61, 72]

$$\Omega_0 = \Omega_0(T = 0, V, \mu) \tag{43}$$

$$= \langle \hat{H}_{\rm kin} + \hat{H}_{\rm chem} + \hat{H}_{\rm int} \rangle \tag{44}$$

$$= \frac{1}{\mathcal{N}} \sum_{\mathbf{k}\alpha} \xi^0_{\mathbf{k}\alpha} \left(1 - \theta^{\alpha}_{\mathbf{k}}\right) - U \sum_{\alpha} \left(\frac{n_{\alpha}}{2}\right)^2 - \frac{1}{U} \sum_{\alpha} |\Delta_{\alpha}|^2, \tag{45}$$

where $\xi^0_{\mathbf{k}\alpha} = \epsilon_{\mathbf{k}\alpha} - \mu$. The electron density, n_{α}, and the superconducting energy gap, Δ_{α}, for the band α are self-consistently determined by the density equation

$$n_{\alpha} = \frac{1}{\mathcal{N}} \sum_{\mathbf{k}} \left(1 - \cos\theta^{\alpha}_{\mathbf{k}}\right), \tag{46}$$

and the gap equation

$$\Delta_{\alpha} = {\rm e}^{i\phi} \frac{U}{\mathcal{N}} \sum_{\mathbf{k}} \frac{1}{2} \sin\theta^{\alpha}_{\mathbf{k}}. \tag{47}$$

By calculating the functional derivative of Ω_0, the saddle-point solution is given by

$$\frac{\delta\Omega_0}{\delta\theta^{\alpha}_{\mathbf{k}}} = 0, \tag{48}$$

which yields

$$\theta^{\alpha}_{\mathbf{k}} = \tan^{-1}\left(\frac{|\Delta_{\alpha}|}{\xi_{\mathbf{k}\alpha}}\right), \tag{49}$$

where $\xi_{\mathbf{k}\alpha} = \xi^0_{\mathbf{k}\alpha} - Un_\alpha/2$. By using the gapped quasi-particle energy spectrum

$$E_{\mathbf{k}\alpha} = \sqrt{\xi^2_{\mathbf{k}\alpha} + |\Delta_\alpha|^2}, \tag{50}$$

the density and gap equations become

$$n_\alpha = \frac{1}{\mathcal{N}} \sum_{\mathbf{k}} \left(1 - \frac{\xi_{\mathbf{k}\alpha}}{E_{\mathbf{k}\alpha}}\right) \tag{51}$$

$$|\Delta_\alpha| = \frac{U}{\mathcal{N}} \sum_{\mathbf{k}} \frac{|\Delta_\alpha|}{2E_{\mathbf{k}\alpha}}, \tag{52}$$

respectively, and we obtain the saddle-point free energy

$$\Omega_0 = \frac{1}{\mathcal{N}} \sum_{\mathbf{k}} \xi^0_{\mathbf{k}\alpha} \left(1 - \frac{\xi_{\mathbf{k}\alpha}}{E_{\mathbf{k}\alpha}}\right) - U \sum_\alpha \left(\frac{n_\alpha}{2}\right)^2 - \frac{1}{U} \sum_\alpha |\Delta_\alpha|^2. \tag{53}$$

The gap equation always has a normal state solution of $|\Delta_\alpha| = 0$, while a superconducting solution has none-zero gap energy, $|\Delta_\alpha| \neq 0$. It is not always obvious whether a superconducting solutions has a lower energy, as discovered in Graphene[67–69], due to vanishing DOS at Dirac points. In the grand canonical ensemble with variable number of electrons, the state with the lowest thermodynamic potential energy $\Omega_0(T = 0, V, \mu)$ will be realised at the given chemical potential, μ. For the fixed number of electrons, N_e, or equivalently, at the fixed density, $n = N_\mathrm{e}/\mathcal{N}_\mathrm{tot}$, on the other hand, we need to find out a state with the lowest Helmholtz free energy, whose zero-temperature form is given by the internal energy

$$F_0 = F_0(T = 0, V, n) \tag{54}$$

$$= \langle \hat{H}_\mathrm{kin} + \hat{H}_\mathrm{int} \rangle. \tag{55}$$

The difference between $\Omega_0(T = 0, V, \mu)$ and $F_0(T = 0, V, n)$ was crucial to identify the correct ground state.

At finite temperature, $T \neq 0$, we can use a standard Bogoliubov transformations[3, 4, 6, 7, 61, 72] to obtain the self-consistency conditions

$$n_\alpha = \frac{1}{\mathcal{N}} \sum_{\mathbf{k}} \left(1 - \frac{\xi_{\mathbf{k}\alpha}}{E_{\mathbf{k}\alpha}} \tanh\left(\frac{\beta E_{\mathbf{k}\alpha}}{2}\right)\right) \tag{56}$$

$$|\Delta_\alpha| = \frac{U}{\mathcal{N}} \sum_{\mathbf{k}} \frac{|\Delta_\alpha|}{2E_{\mathbf{k}\alpha}} \tanh\left(\frac{\beta E_{\mathbf{k}\alpha}}{2}\right), \tag{57}$$

where $\beta = 1/(k_\mathrm{B}T)$ with the Boltzmann constant of k_B, and the thermodynamic potential becomes

$$\Omega = \Omega(T, V, \mu) \tag{58}$$

$$= \frac{2}{\mathcal{N}} \sum_{\mathbf{k}} E_{\mathbf{k}\alpha} \frac{1}{\mathrm{e}^{\beta E_{\mathbf{k}\alpha}} + 1} - \frac{1}{\mathcal{N}} \sum_{\mathbf{k}} (E_{\mathbf{k}\alpha} - \xi_{\mathbf{k}\alpha})$$

$$+ U \sum_{\alpha} \left(\frac{n_\alpha}{2} \right)^2 + \frac{1}{U} \sum_{\alpha} |\Delta_\alpha|^2, \tag{59}$$

whose first term vanishes towards $T = 0$, corresponding to the disappearance of a quasi-particle, which is the main reason for zero resistivity and the Meissner effect, because the absence of single particle excitation leads to the macroscopic coherence, characterised by the current proportional to the vector potential[3–6].

3. Results and discussions

3.1. Ground state solutions and quantum critical behaviours

Numerical solutions of self-consistency equations at $T = 0$ are shown in Fig. 9. The non-doped $(2, 2)$-Hopfene is half-filled ($n = 1$), and it is semi-metal at $U = 0$ (Figs .8 and 9 (a)). With the introduction of $U \neq 0$, Δ_3 developed with the peak at $U \sim 3$ eV (Fig. 9 (b)) and it decreased upon increasing U. This was attributed to the reduction of the filling fraction of n_3 due to the decrease of the effective lower band energy of $\xi_{\mathbf{k}2} = \epsilon_{\mathbf{k}2} - Un_2/2$ by the Hartree-Fock interaction. Consequently, the $\epsilon_{\mathbf{k}3}$ band becomes empty at $U > U_{\rm MI} \sim 4$ eV, and Δ_3 vanishes, and we expect a Metal-Insulator transition in the normal state at $U_{\rm MI}$ due to the opening of the semiconductor gap. With sufficient doping, such significant changes in the filling fractions were not found in a system (Fig. 9 (b)). On the other hand, Δ_2 remained to be zero at $n = 1$ until $U_{\rm c} \sim 1$ eV, showing that the system is very close to the quantum critical point[67–69]. At $U < U_{\rm c}$, the free energy is lower by reducing $\xi_{\mathbf{k}2}$ without opening Δ_2, which is similar to the finding of the quantum critical behaviour in $2D$ Graphene. However, in Hopfene, the DOS is finite at $\mu \sim 1$ eV (Figs. 8 and 9 (e)) and the reduction in the mean-field Hartree-Fock energy overcame the emergence of superconducting order. Surprisingly, further increase of $U > U_{\rm MI}$ allowed the increase of Δ_2, although the increase is significantly smaller than that in the doped case at $n = 1.25$ (Fig. 9 (d)). This increase of Δ_2 at $n = 1$ is similar to the pioneering work found in Ref. [65], where the superconducting order is expected in a semiconductor with a small band gap, if the attractive interaction between electrons in conduction band and holes in valence band is strong enough to overcome the semiconductor gap. An excitonic strong pairing and condensation were experimentally found in Graphite under extremely high magnetic fields in the quantum limit[66]. In our case, the attractive interaction is working within the sub-bands, and the opening of the superconducting gap Δ_2 is smaller than the semiconductor gap $\sim U$. Consequently, the energy gain by the superconducting order at $n = 1$ was significantly limited.

The condensation energies were calculated by the difference of the Helmholtz free energy between superconducting and normal state, $\Delta F = F_{\rm super} - F_{\rm normal}$ (Fig. 10). At $n = 1$, we estimated solely from the BCS theory (Fig. 10 (a)), because the band is almost completely filled and the impact of strong correlation is limited. In fact, ΔF was order of magnitude smaller than that in the doped case (Fig. 10 (b)), so that the system at $n = 1$ is closer to a band insulator. In particular, $\Delta F \sim 0$ at $U \sim U_{\rm MI}$, where Δ_3 is

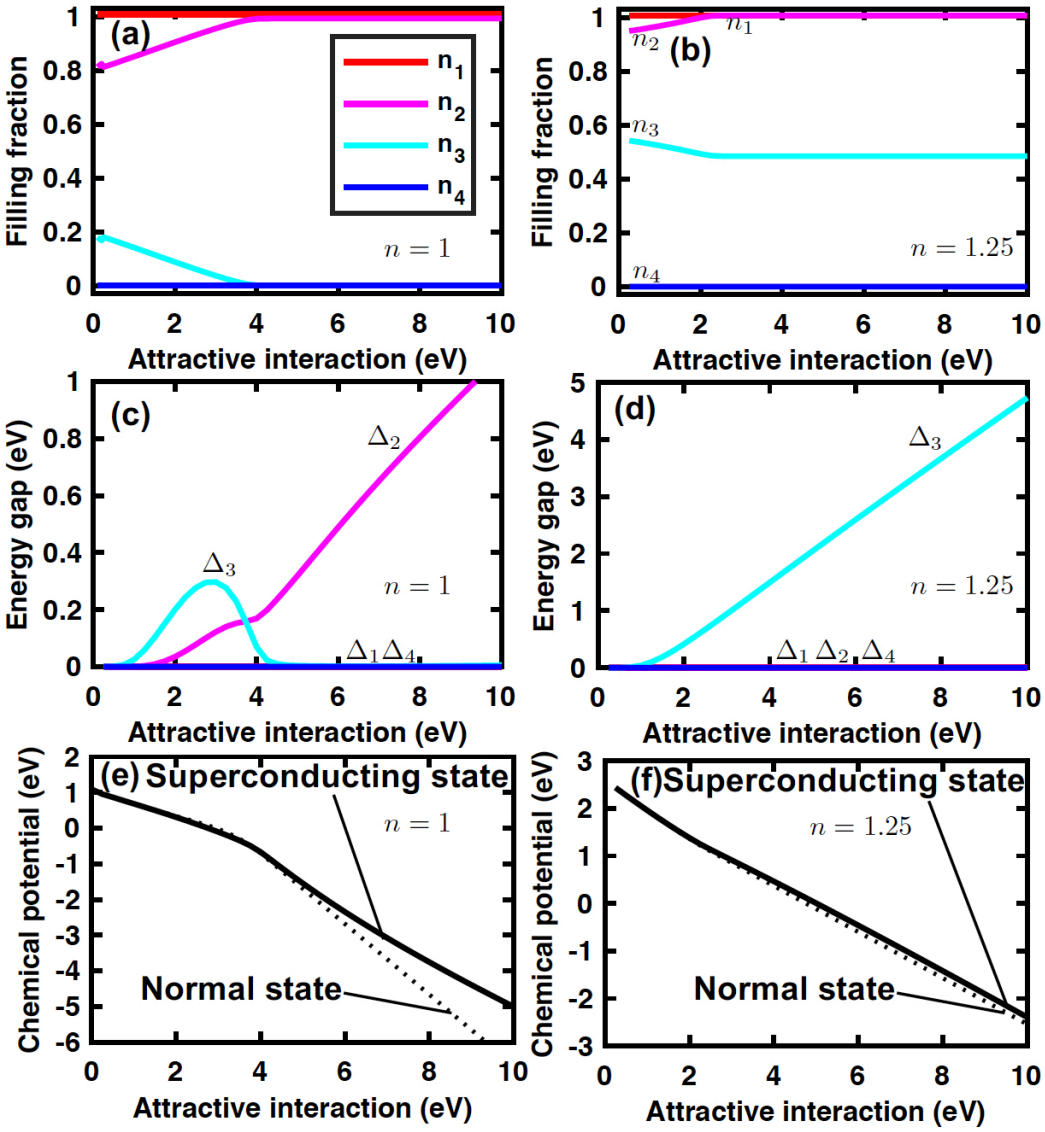

Figure 9. Superconducting ground state of (2,2)-Hopfene. (a)(b) Filling fractions, (c)(d) energy gap, and (e)(f) chemical potential at $n = 1$ and $n = 1.25$, respectively. Reentrant behaviour was found in Δ_3 in (c) due to the opening of the semiconductor gap by the Hartree-Fock interaction.

also close to zero. On the other hand, the BCS theory overestimates ΔF for $n = 1.25$ at the strong coupling limit. It is beyond the scope of this paper to include the impact of strong correlation precisely, because it is quite challenging to include small energy scale of the order t^2/U, which is similar to the problem of Mott transition[61]. Here, we roughly estimate the impact of strong correlation by considering a Gutzwiller-BCS variational wavefunction[64, 73, 74]

$$|\mathrm{GBCS}\rangle = \prod_i [1 + (g-1)n_{i\uparrow}n_{i\downarrow}]\,|\mathrm{BCS}\rangle, \tag{60}$$

by which local spatial correlation is included in the limit of $g \to \infty$ [64, 74]. In this

limit, the electrons are spreading completely in the momentum space to form local singlet of preformed electrons. The impact of the correlation on the free energy in a superconducting state is actually not significant, while the change in the normal state is significant[64]. Therefore, we estimated the normal state free energy simply by assuming all electrons to form locally singlet pairs with the interaction energy of $-Un/2$, while the kinetic energy was calculated by assuming local paring corresponds to the spreading in the entire sub-band in momentum space[64, 74]. The calculated condensation energy is considered to be a simplified BEC model, which is shown in Fig. 10 (b). We could somehow include the energy scale of t^2/U, and the true condensation energy would show a crossover from BCS to BEC.

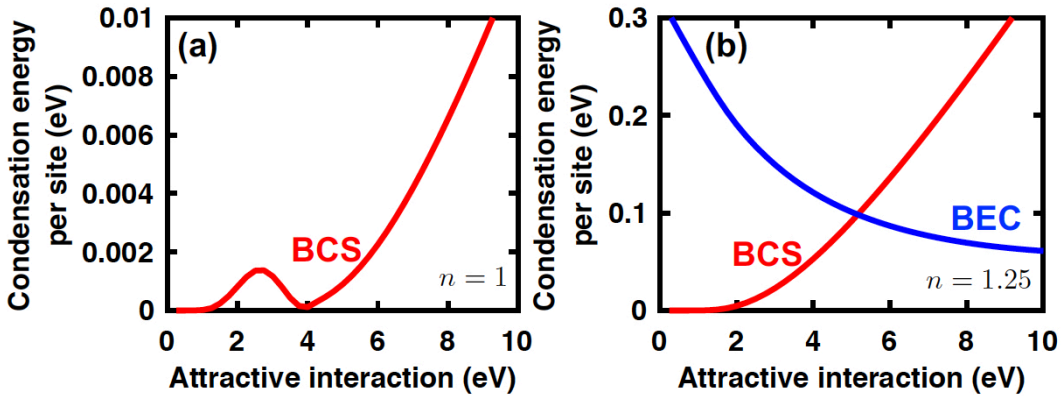

Figure 10. Superconducting condensation energies at (a) $n = 1$ and (b) $n = 1.25$. (a) Superconducting order is significantly limited by the opening of the semiconductor gap. (b) Smooth crossover from weak coupling BCS to strong coupling BEC.

We have also examined the filling dependence of superconductivity in $(2, 2)$-Hopfene (Fig. 11). We found significant decreases of superconducting order parameters at every quarterly fillings (Figs. 11 (a), (c), and (e)), because of the complete filling of the lower sub-bands. These observations are consistent with the filling fractions found in Figs. 11 (b), (d), and (f), which show the subsequent completion of filling at $n = 0.5, 1, 1.5$ and 2, so that the system is close to quantum critical points towards a semiconductor or an insulator. At $n = 1$, it was quite marginal whether the superconducting order remains, as we have seen in Figs. 9 and 10, and according to our numerical calculations, the system remains to be superconducting at $T = 0$. The robust superconductivity at $n = 1$ was coming from the sharp peak of the sub-band ϵ_3 at the bottom edge of the band, because of the flat-band (Fig. 5(c)). At $n = 0.5$, the superconducting order parameters are reduced even further, which was coming from the stronger confinement of $3D$ Weyl Fermions at the top edge of the sub-band ϵ_1 (Fig. 5(d)). Therefore, the system at $n = 0.5$ in the strong coupling is very close to the situation of the reduced superconductivity found in $2D$ Dirac Fermions[67–69]. In our case, the system is semi-metal with the finite DOS from sub-bands ϵ_1 and ϵ_2 at the weak coupling, so that the superconducting order is still finite and there is no finite critical attractive interaction

strength to induce the superconductivity. In that sense, from fundamental point of view, superconductivity in $3D$ Hopfene is less significant compared with the case in $2D$ Graphene. This is consistent with the common understanding, that order parameters are more robust against quantum and thermal fluctuations in higher dimensions, where mean-field pictures are validated[11, 13, 35, 37]. Nevertheless, at strong coupling, the Hartree-Fock interaction reduces the sub-band energy, effectively, leading to an isolation of ϵ_1 and opening of a semiconductor gap.

The superconducting energy gaps were significantly affected by DOS (Figs. 11 (e) and Fig. 8) at weak coupling, as expected from the BCS theory. On the other hand, in the strong coupling, the gaps are smooth functions of fillings (Figs. 11 (a) and (c)), showing the states are spreading to the entire Brillouin zone of the momentum space in order to form local singlet pairs, so that the system is close to BEC.

3.2. Crossover from BCS to BEC and superconductor-insulator phase transition

We have also examined the temperature dependence of superconducting order parameters by solving the self-consistency conditions, Eqs. (56) and (57), simultaneously. We found continuous reductions of order parameters as we increase the temperature, so that the phase transitions are of the second order. This is expected in a $3D$ material, for which the mean field theory should be appropriate. Superconductivity is considerably reduced at $n = 1$, while it is order of magnitude larger at $n = 1.25$, consistent with previous results. Obviously, the superconducting transition temperatures are too large if we assume $U > 2$ eV. In practice, superconductivity in carbon allotropes[15, 16, 56, 57, 60] were found only at temperatures much lower than room temperature. Therefore, a weak coupling condition $U < 1$ eV is appropriate, when we consider realistic experiments. Nevertheless, it would be valuable to consider a crossover[61] or a possible quantum phase transition[19, 64] at least theoretically. Stronger coupling would be expected to excitonic systems[66], for which the model needs to be modified to allow the inter-band interactions.

Finally, we have made phase diagrams of $(2, 2)$-Hopfene based on an attractive Hubbard model (Fig. 13). At $n = 1$, which would be expected for non-doped Hopfene, we expect BCS superconductivity with reduced transition temperatures. In the weak coupling limit, only Δ_3 opens up. At moderate interaction strengths, $1 \text{ eV} < U < 4 \text{ eV}$, both Δ_2 and Δ_3 open at low temperature. At strong coupling limit $U > 4$ eV, we expect insulator to superconductor transition at high temperature, because of the opening of a semiconductor gap, solely from the attractive Hartree-Fock interaction, which is different from Mott transition coming from strong correlation. Obviously, the transition temperature of the order 1000 K is not realistic at all, since Hopfene would be burned out. Nevertheless, we hope there is some theoretical implications of this result, since our results suggest competitions of a semiconductor band gap and a superconducting energy gap with an increase of attractive interaction strength, which is similar to a problem suggested by Nozières and Pistolesi[65]. At $n = 1.25$ with sufficient doping, we confirmed

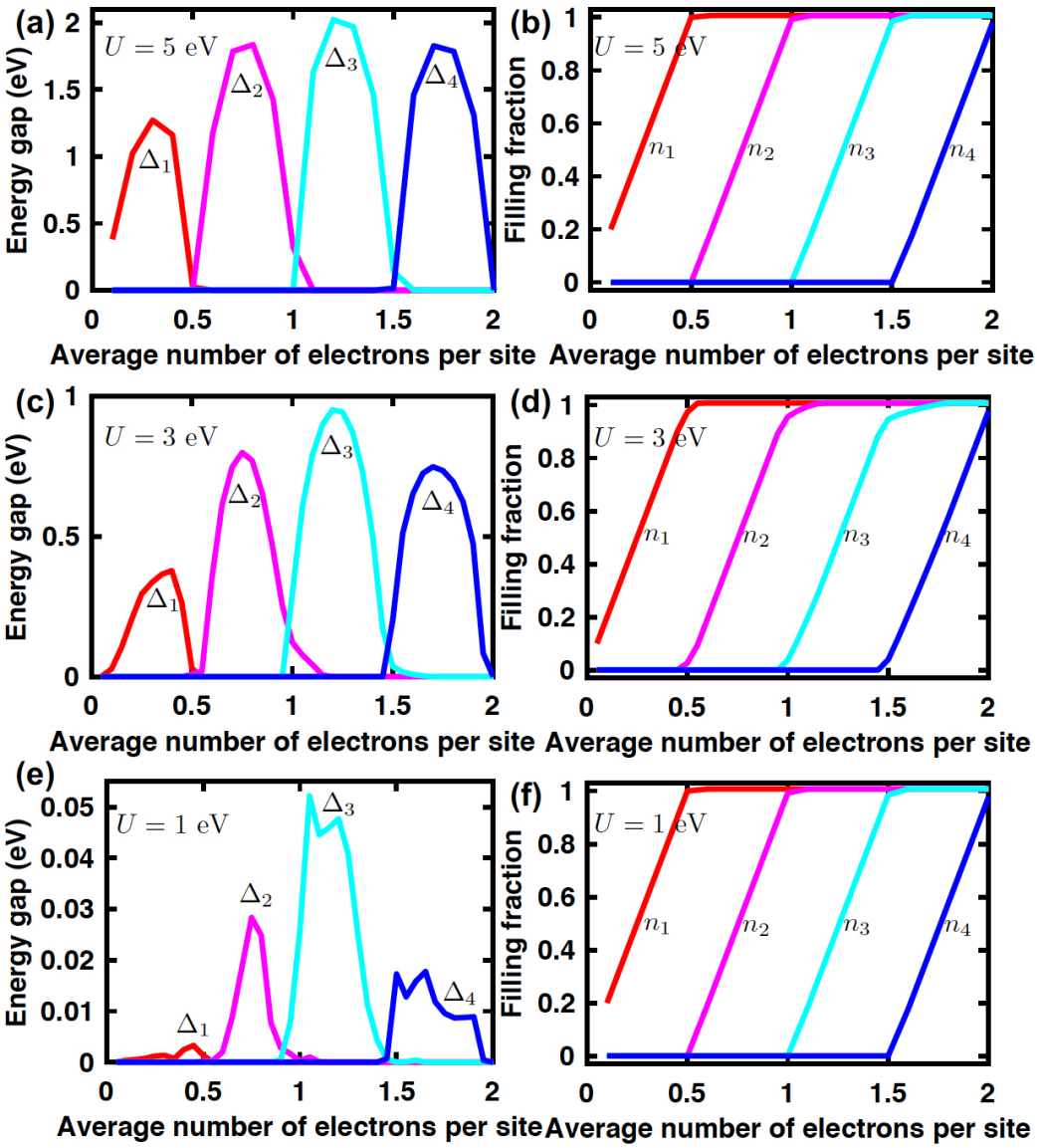

Figure 11. Impact of carrier doping on superconducting order parameters. (a,c,e) Energy gaps and (b,d,f) filling fractions were calculated at $U = 5, 3$, and 1 eV, respectively. (e) The energy gaps reflects the shape of the density-of-states at weak coupling, while (a,c) they become smooth function against filling at strong coupling due to the spreading of the states in momentum space due to local spatial correlation.

a smooth crossover from BCS to BEC (Fig. 13 (b)). The transition temperature of BEC was simply estimated from the condensation energy, so that it is not accurate quantitatively. Nevertheless, the result suggests the existence of the optimum interaction strength at around $U \sim 2$ eV, so that the infinitely strong attraction would not help to increase transition temperature, which is consistent with previous publications[61]. The gap formation is important at weak coupling to expect superconductivity, while the phase coherence is required to expect BEC of local singlet pairs. The sharp increase in

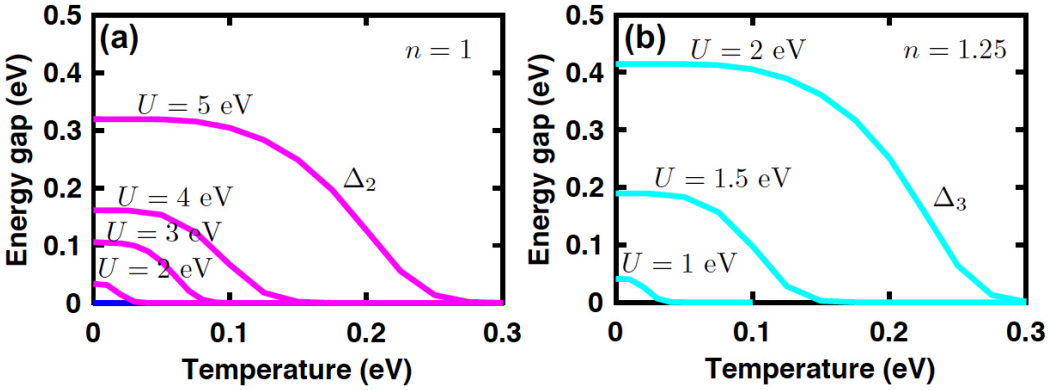

Figure 12. Temperature dependence of order parameters at (a) $n = 1$ and (b) $n = 1.25$. They show the second order phase transition.

DOS by a flat-band will also help to increase the transition temperature at practical weak coupling, while it is less effective due to the spreading in momentum space at strong coupling. The impact of doping on superconductivity in Hopfene is significant and the system is located to the close proximity of the quantum critical point, where the transition temperature is reduced to zero, due to the competition between the opening of semiconductor and superconducting gaps.

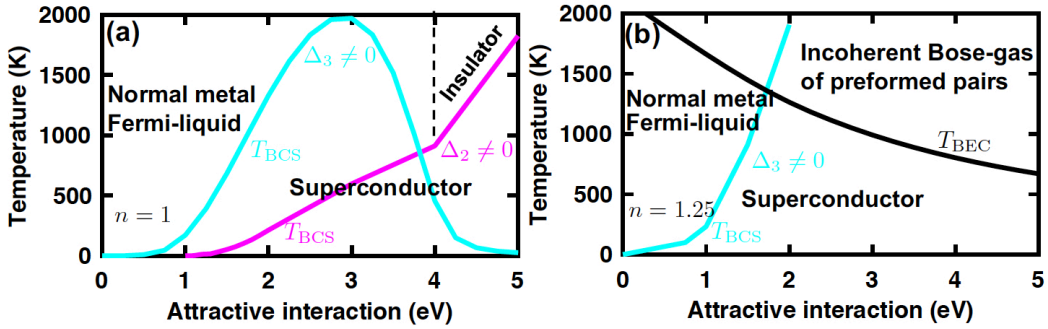

Figure 13. Phase diagrams of attractive Hubbbard model for (2,2)-Hopfene at (a) $n = 1$ and (b) $n = 1.25$. (a) Standard BCS superconductivity is expected at weak coupling, while superconductor to insulator phase transition is expected at strong coupling. (b) Smooth crossover is expected from BCS to BEC. Preformed pairs would behave as Bose-gas at strong coupling at high temperature, and BEC is expected at lower temperature due to the phase coherence. The transition temperature was estimated from the condensation energy.

4. Conclusion

In conclusion, we have proposed a $3D$ carbon allotrope named Hopfene, which has a topologically nontrivial structure with arrays of Hopf-links to link $2D$ Graphne layers, and examined possible superconductivity based on an attractive Hubbard model. We

found topologically unique Fermi surfaces with Dirac and Weyl Fermisons and flat-band features, which affected significantly on the nature of superconductivity especially at practical weak coupling limit. We also found the superconductivity is significantly reduced at every quarterly fillings, due to the opening of semiconductor band gaps, so that the system is in the vicinity of the quantum critical point. As we increase the interaction strength, we confirmed smooth crossover from weak coupling BCS superconductivity to BEC in a doped system. At the half-filling without doping, the superconductivity is significantly reduced and a superconductor-insulator transition was found at the strong coupling limit.

We think unique topological features of Hopfene are valuable to investigate impacts of topology and Fermi surfaces on the emergence of various order parameters including superconductivity, charge-density-waves, magnetisms, and so on. For magnetisms, e.g., we expect ferro-magnetism[7] due to the flat-bands and the peaks in DOS by the introduction of Coulomb repulsive interaction. We also expect introduction of frustration of anti-ferro-magnetic orders through Hopf-links. The impacts of topological structures on magnetism would be quite interesting to explore. Our theoretical analysis in this paper is quite primitive, and we would like to encourage researchers to explore Hopfene and other topologically unique carbon allotropes towards the paradigm-shift of material science and innovation.

Acknowledgments

This work is supported by EPSRC Manufacturing Fellowship (EP/M008975/1). We would like to thank Prof. H. Mizuta, Dr. M. Muruganathan, Prof. Y. Oshima, Prof. S. Matsui, Prof. S. Ogawa, Prof. S. Kurihara, and Prof. H. N. Rutt for stimulating discussions. S.S also would like to thank JAIST for their hospitalities during his stay at the Center for Single Nanoscale Innovative Devices. The data from the paper can be obtained from the University of Southampton ePrint research repository: https://doi.org/10.5258/SOTON/D0955.

[1] Onnes H K 1911 *Comm. Phys. Lab. Univ. Leiden. Suppl.* **29**
[2] v Delft D and Kes P 2010 *Phys. Today* **63** 38–42
[3] Bardeen J, Cooper L N and Schrieffer J R 1957 *Phys. Rev.* **108** 1175–1204
[4] Schrieffer J R 1971 *Theory of Superconductivity* (Westview Press)
[5] Abrikosov A A, Gorkov L P and Dzyaloshinski I E 1975 *Methods of Quantum Field Thoery in Statistical Physics* (Dover)
[6] Tinkham M 2004 *Introduction to Superconductivity* (Dover)
[7] Lévy L P 1997 *Magnetism and Superconductivity* (Springer)
[8] Nambu Y 1960 *Phys. Rev.* **117**
[9] Anderson P W 1958 *Phys. Rev.* **112** 1900–1916
[10] Goldstone J, Salam A and Weinberg S 1962 *Phy. Rev.* **127** 965–970
[11] Nagaosa N 1999 *Quantum Field Theory in Condensed Matter Physics* (Springer)
[12] Wen X G 2004 *Quantum Field Theory of Many-Body Systems* (Oxford University Press)
[13] Altland A and Simons B 2010 *Condensed Matter Field Theory* (Cambridge University Press)
[14] Bednorz J G and Müller K A 1986 *Z. Physik B - Condensed Matter* **64** 189–193
[15] Hebard A F, Rosseinsky M J, Haddon R C, Murphy D W, Glarum S H, Palstra T T M, Ramirez A P and Kortan A R 1991 *Nature* **350** 600–601
[16] Bbhaumik A, Sachan R, Gupta S and Narayan J 2017 *ACS NANO* **22** 11915–11922
[17] Drozdov A P, Kong P P, Minkov V S, Besedin S P, Kuzovnikov M A, Mozaffari S, Balicas L, Balakirev F F, Graf D E, Prakapenka V B, Greenberg E, Knyazev D A, Tkacz M and Eremets M I 2019 *Nature* **569** 528–531
[18] Lee P A, Nagaosa N and Wen X G 2006 *Rev. Mod. Phys.* **78** 17–85
[19] Vojta M 2003 *Rep. Prog. Phys.* **66** 2069–2110
[20] Ando T, Fowler A B and Stern F 1982 *Rev. Mod. Phys.* **54** 437–672
[21] Kittel C 2004 *Introduction to Solid State Physics* 8th ed (John Wiley & Sons)
[22] Takagi S, Toriumi A, Iwase M and Tango H 1994 *IEEE Trans. Electron Devices* **41** 2357–2362
[23] Fischetti M V and Laux S E 1995 Monte Carlo study of sub-bnad-gap impact ionization in small silicon field-effect transistors *Int. Electron Devices Meeting* (IEEE) pp 305–308
[24] Saito S, Torii K, Shimamoto Y, Tonomura O, Hisamoto D and Onai T 2005 *J. Appl. Phys.* **98** 113706
[25] Saito S, Hisamoto D, Kimura Y, Sugii N, Tsuchiya R, Torii K and Kimura S 2006 Origin of drivability enhancement in scaled pmosfets with 45° rotated $< 100 >$ channels *VLSI Technology, Digest of Technical Papers. Symposium on* pp 150–151
[26] Ootsuka F, Wakahara S, Ichinose K, Honzawa A, Wada S, Sao H, Ando T, Ohta H, Watanabe K and Onai T 2000 A highly dense, high-performance 130nm node cmos technology for large scale system-on-a-chip applications *Int. Electron Devices Meeting* (IEEE) pp 575–578
[27] Ghani T, Armstrong M, Auth C, Bbost M, Charvat P, Glass G, Hoffmann T, Johnson K, Kenyon C, Klaus J, Mclntyre B, Mistry K, Murthy A, Sandford J, Silbberstein M, Sivakumar S, Smith P, Zawadzki K, Thompson S and Bohr M 2003 A 90nm high volume manufacturing logic technology featuring novel 45nm gate length strained silicon cmos transistors *Int. Electron Devices Meeting* (IEEE) pp 112–114
[28] Oshima C and Nagashima A 1997 *J. Phys.: Condens. Metter* **9** 1–20
[29] Ando T 2005 *J. Phys. Soc. Jpn.* **74** 777–817
[30] Novoselov K S, Geim A K, Morozov S V, Jiang D, Zhang Y, Dubonos S V, Grigorieva I V and Firsov A A 2004 *Science* **306** 666–669
[31] Novoselov K S, Geim A K, Morozov S V, Jiang D, Katsnelson M I, Grigorieva I V, Dubonos S V and Firsov A A 2005 *Nature* **438** 197–200
[32] Ferrari A C, Meyer J C, Scardaci V, Casiraghi C, Lazzeri M, Mauri F, Piscanec S, Jiang D, Novoselov K S, Roth S and Geim A K 2006 *Phys. Rev. Lett.* **97** 187401
[33] CastroNeto A H, Guinea F, Peres N M R, Novoselov K S and Geim A K 2009 *Rev. Mod. Phys.* **81** 109–162

[34] Wallace P R 1946 *Phys. Rev* **71** 622–634
[35] Mermin N D and Wagner H 1966 *Phys. Rev. Lett.* **17** 1133–1136
[36] Berezinskii V L 1971 *Soviet Phys. JETP* **32** 493–500
[37] Kosterlitz J M and Thouless D J 1972 *J. Phys. C: Solid State Phys.* **5** L124–L126
[38] Koshino M and ando T 2006 *Phys. Rev. B* **73**
[39] Armitage N P, Mele E J and Vishwanath A 2018 *Rev. Mod. Phys.* **90**
[40] Pancharatnam S 1956 *Proc. Indian Acad. Sci., Sect. A* **44** 247–262
[41] Berry M V 1984 *Proc. R. Sco. Lond. A* **392**
[42] Koma A, Sunouchi K and Miyajima T 1985 *J Vac Sci Technol B* **3**
[43] Novoselov K S, Mishchenko A, Carvalho A and CastroNeto A H 2016 *Science* **353** aac9439
[44] Saito S and Tomita I 2019 *arXiv:1904.08107 [cond-mat.mes-hall]*
[45] Hopf H 1931 *Mathematische Annalen* **104** 637–665
[46] MacGillivray L R, Subramanian S and Zaworotko M J 1994 *J. Chem. Soc., Chem. Commun.* **0** 1325–1326
[47] Carlucci L, Ciani G and Proserpio D M 2003 *Coordin Chem Rev.* 247–289
[48] Proserpio D M 2010 *Nature Chem.* **2** 435–436
[49] Bissell R A, Córdova E, Kaifer A E and Stoddart J F 1994 *Nature* **369** 133–137
[50] Fang L, Olson M A, Benítez D, Tkatchouk E, III W A G and Stoddart J F 2010 *Chem. Soc. Rev.* **39** 17–29
[51] v d Molen S J, Liao J, Kudernac T, Agustsson J S, Bernard L, Calame M, v Wees B J, Feringa B L and Schónenberger C 2009 *Nano Lett.* **9** 76–80
[52] Sauvage J P 2017 *Angew. Chem. Int. Ed.* **56** 11080–11093
[53] Dabrowski-Tumanski P and Sulkowska J I 2017 *PNAS* **114** 3415–3420
[54] Saito S and Tomita I 2019 *arXiv:1904.12784 [cond-mat.mes-hall]*
[55] Tomita I and Saito S 2019 *in preparation*
[56] Belash I T, Zharikov O V and Palnichenko A V 1989 *Synthetic Metals* **34** 455–460
[57] Emery N, Hérold C, Marêché J F and Lagrange P 2008 *Sci. Technol. Adv. Mater.* **9** 044102
[58] Kamide K, Kimura T, Nishida M and Kurihara S 2003 *Phys. Rev. B* **68** 024506
[59] Cleuziou J P, Wernsdorfer W, Bouchiat V, Ondarçuhu T and Monthioux M 2006 *Nat. Nanotech.* **1** 53–59
[60] Cao Y, Fatemi V, Fang S, Watanabe K, Taniguchi T, Kaxiras E and Jarillo-Herrero P 2018 *Nature* **556** 43–50
[61] Micnas R, Ranninger J and Robaskiewicz S 1990 *Rev. Mod. Phys.* **62** 113–171
[62] Nozières P and Schmitt-Rink S 1985 *J. Low Temp. Phys.* **59** 195–211
[63] Kamide K and Ogawa T 2011 *Phys. Rev. B* **83** 165319
[64] Saito S, Yoshimoto H, Suzuki Y Y and Kurihara S 2001 *J. Phys. Soc. Jpn.* **70** 1186–1189
[65] Nozières P and Pistolesi F 1999 *Eur. Phys. J. B* **10** 649–662
[66] Akiba K, Miyake A, Yaguchi H, Matsuo A, Kindo K and Tokunaga M 2015 *J. Phys. Soc. Jpn.* **84** 054709
[67] Zhao E and Paramekanti A 2006 *Phys. Rev. Lett.* **97** 230404
[68] Kopnin N B and Sonin E B 2008 *Phys. Rev. Lett.* **100** 246808
[69] Tsuchiya S, Ganesh R and Paramekanti A 2012 *Phys. Rev. A* **86** 033604
[70] Mazzucchi G, Lepori L and Trombbettoni A 2013 *J. Phys. B: At. Mol. Opt. Phys.* **46** 134014
[71] Iwase Y and Takenobu T 2003 *J. Phys.: Condens. Matter* **15** R495–R519
[72] Fetter A L and Walecka J D 2003 *Quantum Theory of Many-Particle Systems* (Dover)
[73] Gutzwiller M C 1963 *Phys. Rev. Lett.* **10** 159
[74] Suzuki Y Y, Saito S and Kurihara S 1999 *Prog. Theor. Phys.* **102** 953–963